Published in Reviews in Mineralogy, Yakymchuk, C., Clark, C., & White, R. W. (2017). Phase Relations, Reaction Sequences and Petrochronology. Reviews in Mineralogy and Geochemistry, 83(1), 13–53. https://doi.org/10.2138/rmg.2017.83.2

2 Phase Relations, Reaction Sequences and Petrochronology

Chris Yakymchuk
Department of Earth and Environmental Sciences
University of Waterloo
Waterloo, Ontario, Canada, N2L 3G1
cyakymchuk@uwaterloo.ca

Chris Clark
Department of Applied Geology
Curtin University
Perth, Western Australia, Australia, 6102

Richard W. White
Earth System Science Research Centre, Institute of Geoscience
University of Mainz
Mainz, Germany, D-55099

INTRODUCTION

At the core of petrochronology is the relationship between geochronology and the petrological evolution of major mineral assemblages. The focus of this chapter is on outlining some of the available strategies to link inferred reaction sequences and microstructures in metamorphic rocks to the ages obtained from geochronology of accessory minerals and datable major minerals. Reaction sequences and mineral assemblages in metamorphic rocks are primarily a function of pressure (P), temperature (T) and bulk composition (X). Several of the major rock-forming minerals are particularly sensitive to changes in P–T (e.g., garnet, staurolite, biotite, plagioclase), but their direct geochronology is challenging and in many cases not currently possible. One exception is garnet, which can be dated using Sm–Nd and Lu–Hf geochronology (e.g., Baxter et al. 2013). Accessory mineral chronometers such as zircon, monazite, xenotime, titanite and rutile are stable over a relatively wide range of P–T conditions and can incorporate enough U and/or Th to be dated using U–Th–Pb geochronology. Therefore,

34 linking the growth of *P–T* sensitive major minerals to accessory and/or major mineral
35 chronometers is essential for determining a metamorphic *P–T–t* history, which is itself critical
36 for understanding metamorphic rocks and the geodynamic processes that produce them (e.g.,
37 England and Thompson, 1984; McClelland and Lapen 2013; Brown, 2014).
38 Linking the ages obtained from accessory and major minerals with the growth and
39 breakdown of the important *P–T* sensitive minerals requires an understanding of the
40 metamorphic reaction sequences for a particular bulk rock composition along a well-constrained
41 *P–T* evolution. Fortunately, the phase relations and reaction sequences for the most widely
42 studied metamorphic protoliths (e.g., pelites, greywackes, basalts) can be determined using
43 quantitative phase equilibria forward modelling (e.g., Powell and Holland 2008). Comprehensive
44 activity–composition models of the major metamorphic minerals in large chemical systems (e.g.,
45 White et al. 2014a) allow the calculation of phase proportions and compositions for a given rock
46 composition along a metamorphic *P–T* path. For accessory minerals, subsolidus growth and
47 breakdown can be modelled in some cases using phase equilibria modelling (e.g., Spear 2010;
48 Spear and Pyle 2010). Suprasolidus accessory mineral behaviour can be investigated by coupling
49 phase equilibria modelling with the experimental results of accessory mineral solubility in melt
50 (Kelsey et al. 2008; Yakymchuk and Brown 2014b). This technique provides a basic framework
51 for interpreting the geological significance of accessory mineral ages in suprasolidus
52 metamorphic rocks.
53 In this chapter, we use phase equilibria modelling techniques to investigate the reaction
54 sequences for three common rock types (pelite, greywacke, MORB) along several *P–T* paths and
55 explore how these sequences relate to accessory mineral growth and dissolution with a particular
56 focus on zircon and monazite and to a lesser extent apatite. First, we review the important major

rock-forming minerals that are used to link metamorphic reaction sequences to trace element chemistries in accessory minerals. Second, we summarize the current understanding of the controls of accessory mineral growth and breakdown in metamorphic rocks during a *P–T* evolution. Third, we use phase equilibria modelling to examine the reaction sequences for common rock types along several schematic *P–T* paths and discuss the implications for petrochronology. Finally, we examine some of the complicating factors for reconciling the behaviour of accessory minerals in natural systems with the predictions from phase equilibria modelling.

MAJOR MINERALS

Understanding the growth and consumption of the major rock-forming minerals is important in accessory mineral petrochronology for four reasons. First, major minerals may contain significant quantities of the essential structural constituents of accessory minerals commonly used as chronometers. In some cases, accessory mineral can grow directly from the breakdown of major minerals. Examples of this are zircon growth from the release of Zr during the breakdown of garnet (Fraser et al. 1997; Degeling et al. 2001) and ilmenite (Bingen et al. 2001). Second, these minerals may represent important repositories for trace elements, and thus the growth and breakdown of major minerals will influence the availability of these elements for incorporation by growing accessory minerals. Third, the major minerals are important hosts for inclusions of accessory minerals. The breakdown of the major minerals may liberate included accessory minerals into the reaction volume of the rock or alternatively may sequester these minerals away allowing their preservation when they would otherwise be consumed in a reaction

sequence (e.g., Montel et al. 2000). Fourth, the microstructural relationships between accessory and major minerals provide context for delineating the *P–T* history of a metamorphic rock.

Garnet and plagioclase are the major minerals most commonly used in petrochronology because of their distinctive trace element behaviour. Linking their growth and breakdown to ages obtained from accessory mineral chronometers requires an understanding of the bulk composition controls on their stabilities. Below, we outline the controls on the growth and breakdown of garnet and plagioclase, which are of particular importance for petrochronology studies. Our focus is on linking mineral growth to metamorphic reactions and we do not discuss the minerals that are important for thermochronology studies (e.g., amphibole, biotite, muscovite, K-feldspar).

Garnet

Garnet is one of the most useful minerals for constraining metamorphic grade and its high density and strong partitioning of cations forms the basis of many useful thermobarometers (e.g., Spear 1995; Caddick and Kohn 2013). It is a common metamorphic mineral for many different protoliths (pelites, mafic rocks, ultramafic rocks, calc-silicates) and has been extensively used in petrochronology studies (e.g., Vance and O'Nions 1990; Vance and Mahar 1998; Harris et al. 2004). Coupling *P–T* estimates from garnet with monazite U–Pb geochronology can also be used to constrain *P–T–t* paths (e.g., Foster et al. 2000; Gibson et al. 2004; Dragovic et al. 2016). Garnet can also be directly dated using Sm–Nd and Lu–Hf geochronology (e.g., Baxter et al. 2013; Baxter et al. 2017, this volume). Although linking *P–T* information from garnet-bearing assemblages with garnet geochronology is very powerful (e.g., Mulcahy et al. 2014; Dragovic et al. 2012, 2015), direct dating of garnet is challenging and is not yet extensively used.

An important control on the stability of garnet during metamorphism is the bulk rock MnO content (e.g., Symmes and Ferry 1992; Mahar et al. 1997; White et al. 2014b). For pelites, higher bulk rock Mn concentrations stabilize garnet at lower temperatures in the greenschist facies and at lower pressure in the amphibolite facies (White et al. 2014b). The ratio of Fe/Mg is also an important control on garnet growth. For example, relatively magnesium-rich pelites have restricted garnet stability fields (e.g., White et al. 2014a) and in very Mg-rich bulk rock compositions garnet may not even grow along common *P–T* paths (e.g., Fitzsimons et al. 2005). Therefore, depending on the bulk composition of the rock, garnet can be first stabilized in the greenschist facies, the amphibolite facies or not at all.

Garnet is the most important major mineral sink for the heavy rare earth elements (HREE) and yttrium in metamorphic rocks (Bea et al. 1994). Accessory minerals such as zircon, monazite, xenotime, apatite, epidote and allanite are also important repositories for the HREE and Y. Thus, the growth and breakdown of garnet plays an important role in the HREE and Y budgets in rocks and links the trace element chemistry of accessory mineral chronometers to the *P–T* information obtained from garnet-bearing metamorphic assemblages (Pyle et al. 2001; Foster et al. 2002; Kohn et al. 2004; Rubatto 2002; Rubatto and Hermann 2007; Taylor et al. 2015). In general, the equilibrium distribution coefficients of the HREE between garnet and zircon are close to unity for Gd to Lu at high temperature (Taylor et al. 2015). For Yttrium, concentrations in monazite are ~1.5 orders of magnitude higher than in garnet (Bea et al. 1994). Xenotime has Y concentrations that are ~2 orders of magnitude higher than in monazite (Pyle et al. 2001). However, in most cases, garnet is substantially more modally abundant than monazite and xenotime and thus the breakdown or growth of garnet will exert first-order controls on the Y and HREE budget of the rock. Zircon and monazite crystallization during garnet growth will

result in relatively low concentrations of HREE and Y in these minerals because these elements are partitioned into garnet. By contrast, garnet breakdown during accessory mineral growth can result in HREE- and Y-enriched trace element concentrations of the new growth zones of accessory minerals (e.g., Rubatto 2002; Foster et al. 2002, 2004).

Plagioclase

Plagioclase is extremely common in metamorphic rocks and is stable over a wide range of *P–T* conditions. Plagioclase breakdown with increasing pressure is an important part of the reaction sequences for high-pressure metamorphic rocks and eclogites. Similar to garnet, plagioclase is commonly a key mineral in thermobarometers that provides important *P–T* information in many different rock types (Ghent 1976; Wu 2015; Molina et al. 2015). For petrochronology, plagioclase (and to a lesser extent K-feldspar) strongly partitions Eu and Sr over the other major rock-forming minerals (e.g., Gromet and Silver 1983). The growth and breakdown of plagioclase can be tied to Eu anomalies in rare earth element patterns of accessory minerals (Rubatto et al. 2013; Holder et al. 2015; Regis et al. 2016). Strontium concentrations have been used to link accessory mineral growth to the timing of plagioclase breakdown; this is a particularity important relationship in ultrahigh pressure metamorphic rocks (Finger and Krenn 2007; Kylander-Clark et al. 2013; Holder et al. 2015).

ACCESSORY MINERALS

Like the major minerals, accessory minerals are involved in the reaction sequence experienced by metamorphic rocks. The behaviour of some accessory minerals used in petrochronology such as epidote, titanite and rutile can be quantified along a *P–T* evolution using

148 phase equilibria modelling. However, the behaviour of zircon and monazite—the most
149 commonly used mineral chronometers—is more difficult to quantify with current phase
150 equilibria modelling techniques (e.g., Spear and Pyle 2010; Kelsey and Powell 2011) as they
151 contain key elements commonly not considered in model chemical systems.
152
153 **Epidote**
154 Epidote is common in low–medium pressure metabasites, metamorphosed intermediate
155 rocks and calc-silicates (e.g., Grapes and Hoskin 2004) as well as in high- to ultrahigh-pressure
156 metamorphic rocks (e.g., Enami et al. 2004). The chemical controls on epidote stability are
157 mainly bulk rock concentrations of Ca and Al as well as f_{O2} (e.g., Enami et al. 2004). The
158 epidote-group minerals can be important repositories for Zr (e.g., Frei et al. 2004; Kohn et al.
159 2015) and LREE in metamorphic rocks (Frei et al. 2004; Janots et al. 2008). Therefore, the
160 breakdown of Zr-rich epidote may have the potential to generate metamorphic zircon. Coupled
161 allanite and epidote breakdown may produce new monazite (e.g., Janots et al. 2008) if there is
162 also a source of phosphorus such as xenotime or apatite.
163
164 **Titanite**
165 Titanite is common in mafic rocks and in some low-grade metasedimentary rocks and it
166 can be used as a barometer in metabasites (e.g., Kapp et al. 2009). An important factor in the
167 stability of titanite is the relative activities of Ca and Al as influenced by the bulk rock ratio of
168 Ca to Al and the accompanying mineral assemblage. High Ca activities favour titanite over
169 ilmenite and high Al activities favour anorthite (and ilmenite) over titanite (Frost et al. 2001).
170 Consequently, titanite is a common mineral in low-Al compositions such as calc-silicate and

mafic rocks whereas aluminous metasedimentary rocks generally have ilmenite as the main Ti-bearing mineral above the greenschist facies.

Titanite can be directly dated using U–Pb geochronology, but there is some uncertainty about the closure temperature for Pb, which is generally considered to be around 600°C (Warren et al. 2012; Spencer et al. 2013; Stearns et al. 2015; Kirkland et al. 2016), depending on cooling rate. Diffusion profiles of trace elements in titanite can be used to determine the timing and duration of cooling (e.g., geospeedometry) and this is covered in more detail in Kohn (2017, this volume). Titanite thermometry uses the Zr concentration of titanite to estimate temperature (Hayden et al. 2008). However, application of this thermometer requires an estimate of titania activity (a_{TiO2}), which, in the absence of rutile, is difficult to constrain and can vary along a metamorphic evolution depending on the reaction sequences and mineral assemblages as discussed below.

Rutile

Rutile is commonly stable in relatively reduced bulk rock compositions (e.g., Diener and Powell 2010) and is particularity useful in high-pressure metamorphic rocks (Zack and Kooijman 2017). Similar to titanite, rutile can be directly dated with U–Pb geochronology (e.g., Mezger et al. 1989; Clark et al. 2000; Zack et al. 2011; Ewing et al. 2015) and it can be used as a geospeedometer (Smye and Stockli 2014). One of the main uses of rutile is as a thermometer that uses the Zr concentration of rutile to estimate temperature (Zack et al. 2004; Watson et al. 2006; Ferry and Watson 2007; Tomkins et al. 2007; Hofmann et al. 2013; Taylor-Jones and Powell 2015). These applications are discussed in more detail by Zack and Kooijman (2017, this volume).

194 Metamorphic reaction sequences with or without rutile have important implications for
195 applying the Ti-in-quartz thermometer (e.g., Chambers and Kohn 2012; Ashley and Law 2015)
196 and the Ti-in-zircon thermometer (e.g., Ferry and Watson 2007), both of which use a_{TiO2} as a
197 variable. In rutile-bearing systems a_{TiO2} is buffered at 1.0. In rutile-absent systems, application of
198 the thermometer requires an estimate of a_{TiO2} that is less that 1.0. Figure 1 shows the difference
199 of calculated temperatures using the Ti-in-quartz thermometer (Wark and Watson 2006) and the
200 Ti-in-zircon thermometer (Ferry and Watson 2007) as a function of temperature for a range of
201 a_{TiO2} values.
202 For example, consider an amphibolite-facies rock at 650°C with a true a_{TiO2} value 0.6. If
203 an a_{TiO2} value of 1.0 is assumed for Ti-in-quartz thermometry, the result would underestimate the
204 true temperature by ~50°C (Fig. 1a). Similarly, using an a_{TiO2} value of 1.0 when the true value is
205 0.6, the Ti-in-zircon thermometer would underestimate the true temperature by ~40°C (Fig 1b).
206 Phase equilibria modelling provides one method of determining a_{TiO2} in metamorphic rocks at
207 different stages of a *P–T* evolution in rutile-absent rocks (e.g., Ashley and Law 2015). We
208 explore this in more detail during our discussion of particular reaction sequences.
209
210 **Zircon**
211 Zircon is the main repository of Zr in most igneous and metamorphic rocks and is the
212 most widely used accessory mineral for U–Pb geochronology (Hoskin and Schaltegger 2003;
213 Rubatto 2017, this volume). Many metamorphic rocks contain relict zircon that may be detrital
214 or igneous in origin and may also be inherited from a previous metamorphic event. For
215 petrochronology, metamorphic zircon can be used to date different portions of a *P–T* evolution
216 depending on the growth mechanisms. The main processes that increase the mode of zircon in

metamorphic rocks include solid-state growth and the crystallization from anatectic melt. In some cases, zircon may precipitate from hydrothermal fluids (e.g., Schaltegger, 2007).

Solid-state zircon growth can occur from the breakdown of other Zr-rich minerals such as garnet (Fraser et al. 1997; Degeling et al. 2001), ilmenite (Bingen et al. 2001), rutile (Ewing et al. 2014) and possibly amphibole (Sláma et al. 2007). This zircon can be used to date major metamorphic assemblage changes during prograde (e.g., Fraser et al. 1997) or retrograde metamorphism (e.g., Degeling et al. 2001) depending on when the Zr-rich mineral breaks down during the reaction sequence. However, major minerals such as garnet, rutile and hornblende can accommodate more Zr as temperature increases and, in general, zircon will be consumed and prograde zircon growth is expected to be limited (Kohn et al. 2015).

The crystallization of anatectic melt typically drives new zircon growth in suprasolidus metamorphic rocks (Watson 1996; Roberts and Finger 1997; Schaltegger et al. 1999; Vavra et al. 1999; Hermann et al. 2001; Kelsey et al. 2008; Yakymchuk and Brown 2014b). Experimental studies show that the concentration of Zr in melt needed to maintain equilibrium with zircon increases with temperature (e.g., Harrison and Watson 1983; Gervasoni et al. 2016) and the compositional parameter *M*, which is the cation ratio of [Na + K + 2Ca]/ [Al x Si] (Watson and Harrison 1983; Boehnke et al. 2013). Generally, the concentration of Zr needed for saturation of intermediate melts (high *M* values) is higher than for more felsic melts (low *M* values). In suprasolidus metamorphic rocks, the most important factor is the amount of anatectic melt present in the system (Kelsey et al. 2008; Kelsey et al. 2011; Yakymchuk and Brown 2014b). As the fraction of melt increases during prograde metamorphism, zircon is expected to break down to maintain Zr saturation of the melt in an equilibrated system. Consequently, prograde zircon growth is expected to be limited above the solidus. In general, melt crystallization during cooling

240 from peak *T* is expected to be the main mechanism for zircon growth in suprasolidus
241 metamorphic rocks. This is supported by ranges of concordant ages that reflect protracted zircon
242 growth during melt crystallization from peak *T* in migmatites (e.g., Korhonen et al. 2013b,
243 2014).

244 New zircon growth can also occur at the expense of pre-existing zircon with no change in
245 the mode of zircon in the rock. Recrystallization of metamict zircon in the presence of a fluid
246 may be an important factor for some prograde zircon (e.g., Rubatto and Hermann 2003; Hay and
247 Dempster 2009). Ostwald ripening has been proposed as a mechanism that could produce
248 prograde growth of zircon in suprasolidus metamorphic rocks (Vavra et al. 1999; Nemchin et al.
249 2001; Kawakami et al. 2013). Ostwald ripening (or second phase coarsening) is a process
250 whereby small solids are preferentially dissolved and precipitate on existing larger solids to
251 reduce the total surface free energy (e.g., Tikare and Cawley 1998). While this process has been
252 studied and debated for the major minerals in metamorphic rocks (Miyazaki 1991, 1996; Carlson
253 1999, 2000) it has not been as extensively studied for accessory minerals—an exception being
254 Nemchin et al. (2001). Nonetheless, it is a possible mechanism for prograde growth of zircon in
255 suprasolidus metamorphic rocks, though involving no net modal increase in zircon.

256 Zircon can also be used as a thermometer in igneous and metamorphic rocks. The Ti-in-
257 zircon thermometer has been increasingly applied to high-temperature metamorphic rocks over
258 the last decade. Kelsey and Hand (2015) compiled Ti-in-zircon temperatures from UHT rocks
259 and noted that 62% of the results fall below the UHT threshold of 900°C. One of the possible
260 reasons for this discrepancy is that some UHT rocks do not contain rutile and are therefore
261 undersaturated in TiO_2 ($a_{TiO2} < 1.0$). Values of a_{TiO2} can range from 1.0 when rutile is in
262 equilibrium with growing zircon to values as low as 0.6 (e.g., Hiess et al. 2008). Using a value of

1.0 when rutile is absent will underestimate the true temperature. Again, the presence and absence of rutile during a reaction sequence has important consequences for applying mineral thermometers in metamorphic rocks.

Monazite

Monazite is generally more reactive than zircon in subsolidus metamorphic rocks and has been extensively used for U–Pb geochronology in aluminous bulk compositions (e.g., Parrish 1990; Engi 2017, this volume). Monazite can be detrital in origin (Smith and Barreiro 1990; Kingsbury et al. 1993; Suzuki et al. 1994; Rubatto et al. 2001), produced through solid-state reactions (e.g., Rubatto et al. 2001; Wing et al. 2003), precipitated from a fluid (e.g., Ayers et al. 1999) or can crystallize from anatectic melt (e.g., Stepanov et al. 2012).

Solid-state monazite growth during prograde metamorphism occurs from the breakdown of LREE-rich precursors, which can include: allanite for high-Ca bulk compositions (Spear and Pyle 2010; Wing et al. 2003; Finger et al. 2016), LREE-rich clays (Copeland et al. 1971), Th or LREE oxides and hydrous phosphates (Spear and Pyle 2002). The most studied solid-state reaction is the growth of monazite at the expense of allanite in bulk compositions with sufficient Ca and LREE to grow allanite at lower grade (e.g., Janots et al. 2008). In natural examples, this reaction has been spatially correlated with the garnet-in isograd (Catlos et al. 2001; Foster et al. 2004), the staurolite-in isograd (Smith and Barriero 1990; Kohn and Malloy 2004; Corrie and Kohn 2008) and the kyanite or sillimanite-in isograds (Wing et al. 2003; Štípská et al. 2015).

Spear (2010) used phase equilibria modelling to examine the *P–T* conditions of the allanite to monazite transition in several bulk rock compositions relative to the average pelite of Shaw (1956). The reaction boundaries for monazite-in at the expense of allanite for these various

compositions are summarized in Figure 2. A higher bulk rock CaO concentration allows allanite to persist to higher temperatures whereas a higher Al_2O_3 concentration stabilizes monazite at lower temperatures. However, the results of this modelling of monazite growth in rocks with variable bulk rock Al_2O_3 concentrations by Spear (2010) are different to those observed in some natural examples. For example, Wing et al. (2003) found that pelites from New England with relatively elevated Ca and/or Al concentrations can preserve allanite to higher temperatures. Gasser et al. (2012) found no link between bulk rock concentrations of CaO and Al_2O_3 and the timing of monazite growth. Therefore, the bulk compositional controls of monazite growth at the expense of allanite are not always clear, but it appears that monazite can grow at a range of temperatures and pressures along a prograde *P–T* path.

The relative amounts of iron and magnesium in a bulk rock composition may also play an important role in the reactions that produce subsolidus monazite. For example, Fitzsimons et al. (2005) showed that monazite in pelitic schists from Western Australia was generated during garnet-breakdown to staurolite and was interpreted to record the timing of peak metamorphism. However, samples that were too magnesium-rich to grow garnet or too iron-rich to grow staurolite at the expense of garnet yielded older monazite ages. Fitzsimons et al. (2005) interpreted these older ages to represent greenschist-facies monazite growth.

In suprasolidus metamorphic rocks, monazite breakdown and growth is controlled mainly by dissolution into and crystallization from anatectic melt. Experimental studies demonstrate that monazite dissolution into melt is a function of temperature, pressure, and the bulk composition of the melt (Montel 1986; Rapp and Watson 1986; Rapp et al. 1987; Skora and Blundy 2012; Stepanov et al. 2012; Duc-Tin and Keppler 2015). The solubility of monazite increases with higher H_2O concentrations in melt (Stepanov et al. 2012) and with decreasing phosphorus

309 concentrations in the melt (Duc-Tin and Keppler 2015). Studies that couple experimentally-
310 determined solubility equations of monazite with phase equilibria modelling show that monazite
311 dissolution increases during prograde metamorphism above the solidus and that for UHT
312 metamorphism most monazite will be completely consumed along the prograde path (Kelsey et
313 al. 2008; Yakymchuk and Brown 2014b). Based on these theoretical models of monazite
314 behaviour, no prograde monazite growth is expected above the solidus. This contrasts with
315 studies of natural rocks that record prograde suprasolidus monazite growth (e.g., Hermann and
316 Rubatto 2003; Hacker et al. 2015). Johnson et al. (2015) suggest that apatite dissolution during
317 prograde metamorphism may have contributed to LREE saturation of the melt and resulted in
318 prograde suprasolidus monazite crystallization. However, the role of apatite breakdown and
319 monazite growth in suprasolidus metamorphic rocks is still poorly understood.
320 Finally, similar to zircon, Ostwald ripening could produce prograde monazite growth in
321 suprasolidus metamorphic rocks (e.g., Nemchin and Bodorkos 2000). However, this has not been
322 extensively studied and may only apply to monazite growth just above the solidus where the
323 modal proportion of anatectic melt is relatively low.
324
325 **Xenotime**
326 Xenotime is a common phosphate in low- to high-grade metamorphic rocks (e.g., Franz
327 et al. 1996; Bea and Montero 1999; Pyle and Spear 1999; Spear and Pyle 2002). It can be
328 directly dated using U–Pb geochronology (e.g., Parrish 1990; Rasmussen et al. 2005, 2007,
329 Sheppard et al. 2007; Janots et al. 2009; Crowley et al. 2009) and can be used as a thermometer
330 when in equilibrium with monazite and garnet (Pyle et al. 2001). Some of the proposed
331 mechanisms of metamorphic xenotime growth are: (1) growth due to dissolution/reprecipitation

of detrital or diagenetic zircon (Dawson et al. 2003; Rasmussen et al. 2011), (2) growth during to the breakdown of detrital zircon (Franz et al. 2015), (3) growth during the breakdown of allanite and/or monazite (Janots et al. 2008), (4) crystallization from anatectic melt (Pyle and Spear 1999; Crowley et al. 2009), and (5) growth during the breakdown of Y-rich garnet (e.g., Pyle and Spear 1999).

There are three important controls on the stability of xenotime in metamorphic rocks. First, higher bulk rock Yttrium concentrations allow xenotime to persist to higher pressures and temperatures (Spear and Pyle 2010). Second, similar to monazite and zircon, partial melting will result in xenotime consumption in order to contribute to REE and P saturation of the melt (e.g., Wolf and London 1995; Duc-Tin and Keppler 2015). Third, xenotime will be consumed during the growth of garnet, which partitions Y and HREE (Pyle and Spear 1999, 2000; Spear and Pyle 2002). Consequently, xenotime in the matrix of high-grade garnet-bearing rocks is relatively rare although xenotime inclusions may be present in garnet (e.g., Pyle and Spear 1999). By contrast, xenotime may be present in the matrix at various metamorphic grades in garnet-absent rocks.

PHASE EQUILIBRIA MODELLING

Phase assemblages in metamorphic rocks generally change through continuous or multivariant reactions rather than discontinuous or univariant reactions (e.g., Stüwe and Powell 1995; Kelsey and Hand 2015). Petrogenetic grids display discontinuous reactions and may yield the false impression that reactions occur over narrow intervals along a *P–T* path (e.g., Vernon 1996). In reality, mineral (and melt) modes and compositions are continuously changing along a *P–T* evolution and these variations represent the reaction sequence of the rock. The particular reaction sequence experienced by a metamorphic rock is dependent on bulk composition, the *P–*

355 *T* path and whether the system is open or closed (e.g., White and Powell 2002; Brown and
356 Korhonen 2009; Yakymchuk and Brown 2014a). The phase assemblages expected for a
357 particular bulk rock composition over a range of *P–T* conditions are commonly depicted using
358 *P–T* pseudosections, phase diagrams constructed for a fixed bulk composition (e.g., Hensen
359 1971; Worley et al. 1998; Spear et al. 2016). More detailed information about the reaction
360 sequences can be determined by using the intersection of a *P–T* path with isopleths (or contours)
361 of different variables (e.g., mineral modes and compositions) on a pseudosection or by
362 constructing mode–temperature or mode–pressure diagrams (e.g., White et al. 2011).
363 Here, we present pseudosections and mode-box diagrams (*P*/*T*–mode plots) for different
364 bulk chemical compositions to investigate the reaction sequences along common *P–T* paths and
365 we discuss the consequences for interpreting the ages obtained from accessory mineral
366 geochronology. The effects of fractionation of growing porphyroblasts and changes in bulk
367 composition are discussed later. Because we use phase equilibria modelling, it is assumed that
368 there are no kinetic controls (e.g., nucleation barriers or sluggish diffusion) that impact the
369 growth or dissolution of major and accessory minerals. Although this assumption may not be
370 strictly valid in some circumstances (Watt and Harley 1993; Pattison and Tinkham 2009; Gaides
371 et al. 2011; Pattison and Debuhr 2015), the modelling here provides a general framework for
372 investigating reaction sequences.
373
374 **Bulk compositions**
375 Three bulk chemical compositions are modelled that represent the most common
376 protoliths investigated during most metamorphic studies. For the subsolidus and suprasolidus *P–*
377 *T* paths, this includes an average amphibolite-facies metapelite (Ague 1991) and an average

passive margin greywacke (Yakymchuk and Brown 2014a). These two compositions were chosen because they are expected to dominate passive margin turbidite sequences that are involved in orogenesis at convergent plate boundaries. A mid-ocean ridge basalt (MORB) from Sun and McDonough (1989) was also used to investigate a suprasolidus reaction sequence for a typical mafic protolith. The modelled bulk compositions are summarized in Table 1. Note that we do not consider melt loss nor fractionation of minerals away from the reacting volume in the modelling here, both of which can modify the composition of the equilibrium volume during a metamorphic evolution (e.g., White and Powell 2002; Evans 2004; Guevara and Caddick 2016; Mayne et al. 2016).

Computational Methods

Forward phase equilibria modelling is used to evaluate the changes to metamorphic mineral assemblages along several schematic *P–T* paths. There are two main approaches to phase equilibria modelling. The first approach is to use Gibbs free energy minimization to determine the stable mineral assemblage at a given *P–T* condition and there are two commonly used software packages available for this approach, including Perple_X (Connolly and Petrini 2002) and Theriak–Domino (de Capitani and Brown 1987; de Capitani and Petrakakis 2010). A second approach is to determine the solution of simultaneous non-linear equations to build up an array of points and lines that make up a metamorphic phase diagram (THERMOCALC: Powell and Holland 1988; Powell et al. 1998; Powell and Holland 2008). Both of these approaches require an internally consistent thermodynamic database derived from the results of experimental studies. There are several commonly-used databases available: Berman (1988), Holland and Powell (1998) and most recently Holland and Powell (2011). Finally, the calculations require

activity–composition models that relate end-member proportions to end-member activities for the solid-solution minerals as well as for complex fluids and melt.

Here, calculations were performed using THERMOCALC v.3.40 (Powell and Holland 1988) using the internally consistent dataset of Holland and Powell (2011). For metapelite and greywacke compositions, modelling was undertaken in the MnO–Na_2O–CaO–K_2O–FeO–MgO–Al_2O_3–SiO_2–H_2O–TiO_2–Fe_2O_3 (MnNCKFMASHTO) chemical system using the activity–composition relations in White et al. (2014a,b). An average MORB composition was investigated in the NCKFMASHTO chemical system using the activity-composition models from Green et al. (2016). Phases modelled as pure end-members are quartz, rutile, titanite, aqueous fluid (H_2O), kyanite and sillimanite. Mineral abbreviations are from Holland and Powell (2011) with the exception of titanite (ttn).

Phase equilibria modelling of subsolidus and suprasolidus systems requires different approaches to approximate the bulk H_2O content of the system. For subsolidus phase equilibria modelling, the amount of H_2O in each bulk composition was set to be in excess, such that a_{H2O} =1. By contrast, suprasolidus rocks are generally not considered to have excess H_2O as the very small amount of free H_2O at the solidus is partitioned into anatectic melt (Huang and Wyllie 1973; Thompson 1982; Clemens and Vielzeuf 1987; White and Powell 2002; White et al. 2005). Along the solidus, the solubility of H_2O in anatectic melt increases with pressure. Therefore, for phase equilibria modelling of suprasolidus rocks, the amount of H_2O in the bulk composition must be set, and was adjusted so that the melt is just saturated with H_2O at solidus at 8 kbar. If the modelled prograde path crossed the solidus at lower or higher pressures, the quantity of melt produced will be slightly overestimated and underestimated, respectively.

Modelled *P–T* paths

Several simplified typical *P–T* paths for subsolidus and suprasolidus systems are modelled to investigate the reaction sequences, changes in mineral modes, amount of melt generated and/or consumed, variations in bulk rock a_{TiO2} and the consequences for interpreting the results of accessory mineral geochronology. Two subsolidus and two suprasolidus *P–T* paths were investigated for the metapelite and greywacke compositions that represent different tectonic evolutions. We also model one suprasolidus *P–T* path for a MORB composition applicable to high-pressure mafic granulites.

For the subsolidus systems, the first *P–T* path has a clockwise trajectory and is representative of collisional orogenesis (e.g., England and Thompson 1984; Thompson and England 1984). An important feature of this *P–T* path is that peak *P* occurs before peak *T*, which is consistent with a relatively long residence time in the core of an orogenic belt. The model path ('clockwise' in Figs 3, 5) contains four segments: (1) heating and burial up to 10 kbar and 550°C, (2) isobaric heating up to 650°C, (3) decompression and minor heating to 8 kbar and 660°C, and (4) decompression and cooling to 6.2 kbar and 610°C.

The second subsolidus *P–T* path has a 'hairpin' trajectory where peak *P* and peak *T* nearly coincide (e.g., 'hairpin' in Figs 3, 5). This style of *P–T* path is also common in collisional orogenesis (e.g., Brown 1998; Kohn 2008) and reflects relatively short residence times at depth and can represent crustal thickening in an accretionary zone of a propagating orogen (Jamieson et al. 2004). The model hairpin *P–T* path contains three segments: (1) heating and burial up to 7 kbar and 610°C, (2) heating and decompression to 6 kbar and 650°C, and (3) decompression and cooling to 4 kbar and 600°C. Peak metamorphism is at the same temperature for both subsolidus *P–T* paths, but the pressures at peak *T* are different.

Two *P–T* paths for suprasolidus rocks that are typical of granulite-facies metamorphism are investigated. First, a clockwise *P–T* path is modelled (e.g., 'clockwise' in Figs 7, 9) that is associated with crustal thickening and heating and is typical of many granulite terranes (e.g., Clark et al. 2011). This *P–T* path contains four segments: (1) increase in pressure and heating across the solidus up to 9 kbar at 850°C, (2) isobaric heating up to 900°C, (3) isothermal decompression to 7 kbar, and (4) cooling and decompression to 5 kbar at 750°C.

Second, a suprasolidus counterclockwise (or anticlockwise) *P–T* path is considered (e.g., 'counterclockwise' in Figs 7, 9) and is common in high temperature–low pressure terranes (e.g., Clarke et al. 1987; Collins and Vernon 1991) and some ultrahigh temperature terrains (e.g., Korhonen et al. 2013a, 2014). This *P–T* path reflects heating prior to thickening (usually at peak *T*) followed by near-isobaric cooling. In some cases, this has been attributed to the inversion of a hot back-arc basin during collisional orogenesis (Clark et al. 2014). The modelled counterclockwise *P–T* path contains four segments: (1) isobaric heating up to 830°C and 5 kbar, (2) heating and an increase in pressure up to 860°C and 6 kbar, (3) cooling and an increase in pressure to 850°C and 7 kbar, and (4) isobaric cooling to 750°C.

A high-pressure clockwise path was also chosen to model the reaction sequences for high-pressure mafic granulites (e.g., O'Brien and Rötzler 2003) and to investigate the growth and breakdown of garnet for these rocks. This *P–T* path contains four segments: (1) heating and an increase in pressure up to 12 kbar and 850°C, (2) isobaric heating up to 950°C, (3) isothermal decompression to 8 kbar, and (4) cooling and decompression to 800°C and 6 kbar. The decompression segments of this *P–T* path are also compatible with the decompression segments of some ultrahigh-pressure metamorphic rocks (Hacker et al. 2010; Chen et al 2013; Xu et al 2013).

Modelling suprasolidus zircon and monazite dissolution

For the suprasolidus *P–T* paths, the growth and dissolution of zircon and monazite are modelled using the method of Kelsey et al. (2008). Note that the bulk composition used in this modelling is fixed without fractionation of elements into growing porphyroblasts (e.g., zirconium into garnet) or loss of melt. These factors are discussed later. First, the saturation concentrations of the melt in ppm are calculated as follows. The major element composition of the anatectic melt is calculated at a specified *P–T*. This composition of the melt is combined with the solubility equations of Boehnke et al. (2013) for zircon and Stepanov et al. (2012) for monazite, and the stoichiometric concentrations of Zr in zircon (497,664 ppm Zr) and LREE in monazite (566,794 ppm LREE) to determine the saturation concentrations of Zr and LREE in ppm (Kelsey et al. 2008). These initial calculations do not account for the proportion of anatectic melt or the bulk-rock concentrations of Zr and LREE. Second, the saturation concentrations of Zr or LREE (ppm) are multiplied by the proportion of anatectic melt in the system (in normalized mol% which is approximately equivalent to vol%) at *P–T* to arrive at concentrations in ppm that are required to saturate the melt in the equilibration volume of the rock. Finally, these values are divided by the assumed bulk-rock chemical concentrations of Zr and LREE. The Zr and LREE in pelites and the greywackes are generally similar to each other and to the values of metasedimentary migmatites; a value of 150 ppm was chosen here (e.g., Yakymchuk and Brown 2014b). For MORB, the Zr concentration was set at 103 ppm, which is an average of global MORB compositions (White and Klein 2014). The sensitivity of these calculations to bulk rock concentrations of Zr and LREE and the assumptions and limitations of this methodology are discussed by Kelsey et al. (2008) and Yakymchuk and Brown (2014b). The result of the

493 calculations is the proportion of zircon or monazite dissolution required to saturate the anatectic
494 melt in Zr and LREE in the equilibration volume of the rock. This value is subtracted from 100%
495 and the results are reported as the percent of zircon and monazite remaining relative to the
496 amounts existing at the fluid-present solidus for each *P–T* path.

497 One important limitation of the monazite saturation equation used here is that it does not
498 account for phosphorus in anatectic melt, which can affect monazite stability (e.g., Duc-Tin and
499 Keppler 2015). The main repository of phosphorus in most metamorphic rocks is apatite, which
500 is expected to break down during partial melting (Wolf and London 1994). Phosphorus
501 saturation in melt is a function of temperature, SiO_2 concentration (Harrison and Watson 1984)
502 and the aluminum saturation index of the melt (ASI = molar $[Al_2O_3]$ / $[K_2O + Na_2O + CaO]$,
503 Wolf and London 1994). The solubility of apatite in melt increases with rising ASI, which is
504 common during prograde partial melting in migmatites (e.g., Johnson et al. 2015). For example,
505 an increase in the ASI from 1.1 to 1.2 increases the solubility of apatite by an order of magnitude
506 (Wolf and London 1994). The breakdown of LREE-rich apatite during prograde metamorphism
507 may contribute to LREE saturation of anatectic melt and monazite crystallization (e.g., Johnson
508 et al. 2015; Rocha et al. 2016). Here, we use melt ASI as a qualitative tool to investigate the
509 behaviour of apatite during partial melting and the consequences for prograde monazite growth
510 in suprasolidus metamorphic rocks.

511

512 **SUBSOLIDUS PHASE RELATIONS AND REACTION SEQUENCES**

513 Phase relations and reaction sequences for two subsolidus *P–T* paths for two bulk compositions
514 are discussed below for a closed system where bulk composition does not change. Fractionation
515 of porphyroblasts away from the reacting volume is not considered in the calculations here.

516

517 **Metapelite**

518 ***Phase relations***. The pseudosection for the amphibolite-facies metapelite is shown in
519 Figure 3. Biotite is stable at $T > 450$–460°C with increasing pressure. Garnet is stable across
520 most of the diagram except at low P and low T and at $P < 5$ kbar just below the solidus. The
521 staurolite-in field boundary extends from 550°C at 4 kbar up to 650°C at 10 kbar. The stability
522 field of the aluminosilicate minerals (kyanite and sillimanite) ranges from $T > 580$°C at 4 kbar to
523 $T > 660$°C at 10 kbar. Rutile is stable at low P at low temperatures and at $P > 10.5$ at $T > 550$°C.

524

525 ***Reaction sequence for the clockwise P–T path***. A mode-box for the reaction sequence
526 for the clockwise P–T path is shown in Figure 4a. During the prograde segment of the clockwise
527 P–T path, chlorite is progressively consumed to produce biotite (starting at 455°C) and then
528 garnet (starting at 460°C). Chlorite is exhausted by 580°C. Rutile is completely consumed by
529 ~530°C. Epidote breaks down along the prograde path and the epidote-out field boundary is
530 encountered at 620°C. The complete breakdown of epidote at 620°C may result in minor zircon
531 crystallization or more likely the growth of new rims on pre-existing zircon.

532 The staurolite stability field is encountered during the heating and decompression
533 segment at 9 kbar and 650°C. In natural examples, prograde monazite growth has been
534 associated with garnet, staurolite and kyanite/sillimanite growth in metapelites (Catlos et al.
535 2001; Smith and Barriero 1990; Wing et al. 2003; Kohn and Malloy 2004; Fitzsimons et al.
536 2005; Corrie and Kohn 2008), although kyanite/sillimanite is not encountered along the P–T path
537 modelled here. In general, monazite could grow at different points along the prograde P–T path.
538 Because garnet growth is predicted to be continuous up to the staurolite-in field boundary, new

539 monazite grown during this segment of the *P–T* path is expected to have low concentrations of
540 HREE and Y; these elements are expected to partition into garnet. Staurolite growth is at the
541 expense of garnet and occurs during the decompression portion of the prograde path (e.g.,
542 Florence and Spear 1993). Monazite formed during this segment is expected to have elevated
543 HREE and Y concentrations due to the breakdown of garnet and the age would record the initial
544 stages of decompression from peak *P*. By contrast, zircon is expected to undergo only minor
545 changes to its mode and will be slightly consumed during subsolidus prograde metamorphism
546 (e.g., Kohn et al. 2015). Two possible exceptions are minor zircon growth during the breakdown
547 of Zr-rich epidote and/or rutile. However, at low temperatures, rutile is not expected to be
548 zirconium rich.

549 The stable mineral assemblage at the metamorphic peak of 660°C and 8 kbar includes
550 garnet, staurolite, biotite, plagioclase, ilmenite, muscovite and quartz. In general, the mode of
551 monazite in metapelites is expected to reach a maximum at peak *P–T* and monazite is not
552 expected to grow during cooling (e.g., Spear and Pyle 2010). An additional factor is that
553 monazite is susceptible to dissolution/reprecipitation in the presence of fluids (e.g., Williams et
554 al. 2011). While fluid-mediated dissolution/reprecipitation should not increase the net mode of
555 monazite, it can occur at almost any point along the *P–T* evolution. Therefore, it is possible that
556 monazite in a subsolidus metapelite can record a range of ages that vary from monazite-in up to
557 the metamorphic peak and dissolution/precipitation may result in ages that record retrogression
558 (Harlov et al. 2005; Williams et al. 2011). On the other hand, zircon is expected to be relatively
559 unreactive and may not record prograde to peak metamorphism in subsolidus metamorphic
560 rocks.

After the exhaustion of rutile during the heating and burial segment the value of a_{TiO2} decreases to 0.95 initially and remains nearly constant until the decompression and heating segment, where a_{TiO2} drops to 0.8. During the subsequent decompression and cooling segment the a_{TiO2} value remains stable at 0.8. After rutile is exhausted, any growth of new zircon or modification of existing zircon will occur when $a_{TiO2} < 1.0$; this needs to be considered when applying the Ti-in-zircon thermometer.

Reaction sequence for the hairpin P–T path. A mode-box for the reaction sequence for the hairpin *P–T* path is shown in Figure 4b. The prograde reaction sequence includes garnet-in at 520°C and 4.5 kbar, staurolite-in at 590°C and 6.5 kbar and sillimanite-in at 640°C and 6 kbar. Garnet both grows and is consumed during the prograde portion of the reaction sequence. The value of a_{TiO2} decreases from 0.88 at 500°C to 0.79 at peak *T*. For the decompression and cooling segment, a small amount of biotite grows at the expense of garnet; the modes of the other minerals are little changed and the a_{TiO2} value remains close to 0.79.

As with the clockwise *P–T* path, monazite growth may occur at various times during the prograde segment of the hairpin *P–T* path. Because the mode of garnet increases and decreases multiple times during the prograde reaction sequence, linking Y and HREE in monazite would be challenging in the absence of microstructural context, such as monazite in coronae surrounding resorbed garnet. For example, HREE and Y-rich monazite could be generated during: (1) the heating and burial segment during garnet breakdown to staurolite, (2) the heating and decompression segment during garnet breakdown to biotite near the metamorphic peak, or (3) garnet breakdown during the retrograde segment of the *P–T* path. Furthermore, xenotime breakdown during prograde metamorphism would also contribute to the growth of Y and HREE-

584 rich monazite with or without a contribution from garnet (e.g., Spear and Pyle 2010). Therefore,
585 for the hairpin *P–T* path modelled here, HREE- or Y-rich monazite can record burial and/or
586 exhumation.
587
588 **Greywacke**
589 ***Phase relations***. The pseudosection for the greywacke is shown in Figure 5. Garnet is
590 stable across the entire diagram. Titanite is stable at $T < 460–470$°C with increasing pressure.
591 Biotite is stable across the diagram except at the high-*P*–low-*T* corner. Chlorite is unstable above
592 600°C at 7 kbar and unstable above 530°C at 12 kbar. Albite is stable below 565°C at 4 kbar and
593 below 620°C at 11 kbar. White mica (muscovite and/or paragonite) is stable up to the solidus at
594 $P > 10$ kbar and at $T < 570$°C at 4 kbar. There are two important sets of quasi-linear field
595 boundaries with positive slopes in *P–T* space. First is the set of boundaries that range from
596 480°C at 4 kbar up to 640°C at 12 kbar represent the breakdown of epidote to produce
597 plagioclase. A second set of fields extends from 570°C at 4 kbar to the solidus with increasing *P*
598 that represent the consumption of paragonite to produce sillimanite or kyanite.
599
600 ***Reaction sequence for the clockwise P–T path***. A mode-box for the assemblage
601 sequence for the clockwise *P–T* path is shown in Figure 6a. For the clockwise *P–T* path the
602 important changes along the prograde reaction sequence include: (1) the growth of rutile
603 commencing at 460°C resulting in a_{TiO2} increasing from 0.9 at 450°C to 1.0 at 460°C, (2) the
604 complete consumption of titanite by 475°C, (3) the growth of biotite and garnet at the expense of
605 chlorite and muscovite from 450°C to 550°C, which results in the complete consumption of
606 chlorite by 550°C, (4) the breakdown of epidote to produce 2 mol% plagioclase at ~605°C, (5)

607 the consumption of ~0.5 mol% garnet to produce plagioclase and hematite from 605°C to 620°C,
608 and (6) the growth of 0.5 mol% garnet from 620°C to 650°C. Similar to the metapelite, the
609 breakdown of Zr-rich epidote may result in minor zircon growth.
610 Decompression and heating from 10 kbar at 650°C to 8 kbar at 660°C results in: (1) the
611 disappearance of rutile at 9.8 kbar and a subsequent drop in a_{TiO2}, and (2) the breakdown of
612 paragonite and garnet to produce kyanite, biotite and plagioclase at 8.8 kbar. The peak
613 metamorphic assemblage at 660°C and 8 kbar includes garnet, kyanite, muscovite, biotite,
614 plagioclase and ilmenite. Further decompression and cooling results in the growth of biotite at
615 the expense of garnet and a gradual decrease in a_{TiO2}.
616 Like the metapelite, garnet breakdown occurs during a portion of the heating and burial
617 segment of the *P–T* path (at ~600°C) and during the heating and decompression segment
618 immediately before the metamorphic peak. Therefore, Y- and HREE-rich monazite associated
619 with garnet breakdown could record the timing of burial and/or exhumation.
620
621 ***Reaction sequence for the hairpin P–T path***. A mode-box for the reaction sequence for
622 the hairpin *P–T* path is shown in Figure 6b. The hairpin *P–T* path has three notable differences in
623 its reaction sequence compared with the clockwise path for the greywacke. First, the *P–T* path
624 does not intersect the epidote stability field. Second, the value of a_{TiO2} is always less than one
625 and decreases from 0.95 to 0.80 along the *P–T* path. And third, white mica is completely
626 consumed by the end of the *P–T* path. In contrast to the multiple garnet growth/consumption
627 segments along the clockwise *P–T* path, the mode of garnet increases during burial and decreases
628 during decompression for the hairpin path. Therefore, Y- and HREE-depleted monazite is

629 predicted to record burial and monazite enriched in these elements would document garnet-
630 breakdown during decompression and/or cooling and may also record xenotime breakdown.
631
632 **SUPRASOLIDUS PHASE RELATIONS AND REACTION SEQUENCES**
633 Phase relations and reaction sequences for three suprasolidus scenarios are discussed below for a
634 closed system where bulk composition does not change and the water content is fixed to just
635 saturate the rock in H_2O at 8 kbar at the solidus. This approach provides important first-order
636 constraints on the reaction sequences for the modelled compositions; it does not take into
637 account melt loss and the associated effects on rock fertility, solidus temperature and zircon and
638 monazite stability. The consequences of open system behaviour on the reaction sequence and
639 accessory mineral stability are discussed later.
640
641 **Metapelite**
642 ***Phase Relations***. The pseudosection for the metapelite is shown in Figure 7. Ilmenite and
643 plagioclase are stable across the entire diagram. Garnet is stable at high pressures across the
644 diagram except at $T < 700$°C at $P < 5.5$ kbar. Cordierite is stable at high-T–low-P conditions.
645 Orthopyroxene is not stable in this diagram. Rutile is restricted to $P > 10$–11.5 kbar across the
646 modelled temperature range. The three important partial melting reactions for the metapelite
647 include: (1) the consumption of any free aqueous fluid to produce melt at the wet solidus, which
648 ranges from 660°C at low pressures to 710°C at high pressure, (2) the incongruent breakdown of
649 muscovite to produce K-feldspar, which is represented by a narrow low-variance field that
650 extends from the wet solidus at low P to $T > 780$°C at $P > 12$ kbar, and (3) the progressive
651 breakdown of biotite at temperatures above the muscovite stability field to produce either garnet

652 at higher pressure or cordierite ± garnet at lower pressure. Biotite is exhausted by 850°C at $P > 7$
653 kbar and melting progresses via the consumption of quartz and feldspar.
654
655 ***Reaction sequence for the clockwise P–T path***. The mode-box and titania activity for the
656 clockwise assemblage sequence are shown in Figure 8a. The predicted amount of monazite and
657 zircon remaining as well as melt ASI are shown in Figure 8b. During the prograde segment of
658 the clockwise *P–T* path, the metapelite begins to melt at the wet solidus at ~680°C through the
659 consumption of any free H_2O as well as quartz and plagioclase. The amount of aqueous fluid at
660 the solidus is expected to be small given the limited porosity of high-grade metamorphic rocks
661 (e.g., Yardley and Valley 1997). Therefore, the amount of melt produced at the wet solidus is
662 expected to be limited. For the modelled metapelite, the amount of melt produced is 4 mol%,
663 although this is mostly an artefact of the modelling which assumes H_2O saturation of the solidus
664 at 8 kbar.
665 After any free H_2O is consumed, partial melting continues with increasing temperature
666 through the consumption of muscovite up until 728°C. This produces an additional 3 mol% melt
667 with a generally constant melt ASI. At 728°C and 7.5 kbar, melting proceeds via the incongruent
668 breakdown of muscovite to generate K-feldspar over a narrow (~2°C) temperature range. This
669 narrow field produces an additional 3 mol% melt. After muscovite is exhausted, the rock
670 contains ~9 mol% melt and approximately 8% of the zircon and 12% of the monazite that was
671 present at the solidus is predicted to have been consumed. A minor amount of apatite breakdown
672 is expected in order to saturate the anatectic melt in phosphorus.
673 After muscovite is completely consumed, partial melting continues through the
674 consumption of biotite, plagioclase and quartz to produce melt, garnet, K-feldspar and ilmenite.

675 This produces an additional 32 mol% melt. Because biotite is an important host of accessory
676 mineral inclusions (e.g., Watson et al. 1989), biotite breakdown may release inclusions of
677 monazite and zircon into the reaction volume of the rock. The liberation of these accessory
678 minerals may contribute to LREE and Zr saturation of the anatectic melt. On the other hand,
679 some zircon and monazite may be included in growing garnet and will be sequestered away from
680 the reaction volume. These minerals will be shielded from dissolution and are more likely to
681 preserve inherited (or detrital) ages as well as any subsolidus to early suprasolidus prograde
682 metamorphic ages. The inclusion of accessory minerals in major minerals effectively reduces the
683 Zr and LREE available to the system and proportionally more zircon and monazite dissolution
684 will be required to maintain melt saturation in these elements (e.g., Yakymchuk and Brown
685 2014b). Therefore, the sequestration of zircon and monazite in stable peritectic minerals such as
686 garnet will promote the dissolution of accessory minerals along grain boundaries in the matrix of
687 the rock with increasing *T*.
688 Titania activity is predicted to reach its highest value of 0.92 at 850°C. At this point, all
689 of the monazite and 85% of the zircon are expected to be consumed. However, during this
690 interval, the ASI of the melt increases from 1.10 to 1.15, which may result in enhanced apatite
691 dissolution. For example, Pichavant et al. (1992) estimate that a similar increase in ASI at 800°C
692 and 5 kbar would change the P_2O_5 concentration of melt from 0.50 to 0.75 wt%. If apatite is
693 LREE rich, the dissolution of apatite may delay the complete dissolution of monazite to higher
694 temperatures or, in extreme cases, may even promote prograde monazite crystallization (e.g.,
695 Johnson et al. 2015).
696 After the complete consumption of biotite, the hydrous minerals have been exhausted and
697 the residuum is essentially composed of anhydrous minerals. Melting continues through the

698 continued consumption of quartz and K-feldspar up to the modelled peak temperature of 900°C.
699 The ASI of the melt reaches 1.18 at peak *T* and significant apatite dissolution is likely. At this
700 point, the metapelite contains 43 mol% melt and both monazite and zircon are absent. After
701 zircon and monazite are completely consumed, further anatexis is expected to generate melt that
702 is undersaturated in Zr and LREE. Therefore, even with the breakdown of LREE-rich apatite,
703 prograde monazite crystallization is not expected above ~850°C.
704 Isothermal decompression from 9 to 7 kbar produces an additional 11 mol% melt at the
705 expense of quartz and K-feldspar. At this point the rock contains the maximum amount of melt
706 of 54 mol%. During this decompression segment, melt ASI increases from 1.18 to 1.23 and a_{TiO2}
707 decreases from 0.86 to 0.74. Approximately 1 mol% garnet is consumed during decompression,
708 which would liberate some HREE and Y into the reaction volume. If significant apatite
709 dissolution occurs and promotes monazite crystallization during decompression, this may be
710 reflected as elevated HREE concentrations in monazite. However, the melt is undersaturated in
711 LREE given the complete exhaustion of monazite at 850°C so new monazite growth is unlikely
712 unless the apatite is very enriched in LREE or the modal proportion of apatite is high.
713 Decompression and cooling from peak *T* results in: (1) melt crystallization, (2) the
714 growth of K-feldspar and quartz until the cordierite stability field is reached at ~880°C and 6.7
715 kbar, (3) garnet and cordierite consumption to produce biotite, (4) new zircon and monazite
716 growth, (5) a decrease in melt ASI and a_{TiO2}. Melt crystallization and cordierite growth are
717 concomitant with the consumption of garnet and sillimanite; this is a common reaction sequence
718 for high-temperature decompression in migmatites. Zircon or monazite produced over this
719 reaction interval is expected to be enriched in HREE and Y (e.g., Yakymchuk et al. 2015).
720 Protracted monazite and zircon growth will occur from peak *T* to the solidus. U–Pb zircon and

721 monazite ages that spread down Concordia have been interpreted to record protracted growth
722 during cooling and melt crystallization in various migmatite terranes with clockwise *P–T*
723 evolutions (Korhonen et al. 2012; Reno et al. 2012; Morrisey et al. 2014; Walsh et al. 2015).
724
725 ***Reaction sequence for the counterclockwise P–T path***. The mode-box and titania
726 activity for the counterclockwise assemblage sequence are shown in Figure 8c. The amount of
727 monazite and zircon remaining as well as melt ASI are shown in Figure 8d. During isobaric
728 heating at 5 kbar, partial melting begins at the wet solidus at ~670°C and continues through the
729 breakdown of muscovite to produce a total 8 mol% melt by 685°C. Melting continues via the
730 progressive breakdown of biotite to produce peritectic garnet and K-feldspar. By 765°C, 17
731 mol% melt is present and roughly 80% and 60% of the initial amount of zircon and monazite,
732 respectively, remains. From the solidus up to 765°C, the a_{TiO2} value of the system has decreased
733 from 0.9 to 0.6 and the ASI of the melt has increased from 1.13 to 1.18. An increase in melt ASI
734 increases the solubility of apatite; this may liberate some LREE and P that could contribute to
735 minor monazite crystallization because the melt is predicted to be saturated with respect to the
736 LREE. Similar to the clockwise *P–T* path, the breakdown of biotite may liberate zircon and/or
737 monazite that was sequestered away from the reacting volume.
738 Cordierite enters the phase assemblage at ~770°C and melting continues through the
739 breakdown of biotite, sillimanite and plagioclase to produce K-feldspar, garnet and cordierite.
740 Sillimanite is completely consumed by 780°C and biotite is exhausted by 800°C. During the
741 interval from 770°C to 800°C, approximately 15 mol% melt is generated and melt ASI decreases
742 slightly from 1.18 to 1.16. Although the change in ASI would decrease the solubility of apatite,

743 this may be counteracted by the additional melt generation during biotite breakdown and apatite
744 growth is not expected.
745 In the absence of biotite, melting continues through the breakdown of quartz, plagioclase
746 and K-feldspar, which results in a progressively drier melt. Monazite and zircon are predicted to
747 be completely consumed by 820°C and 850°C, respectively. The increase in pressure near the
748 metamorphic peak results in minor cordierite consumption to produce garnet. At the
749 metamorphic peak, the metapelite has generated ~44 mol% melt.
750 Isobaric cooling at 6.5 kbar from 860°C to 750°C results in: (1) melt crystallization; (2)
751 new zircon and monazite growth commencing at 855°C and 825°C, respectively; (3) a decrease
752 in melt ASI, which would decrease the solubility of apatite and contribute to apatite
753 crystallization; (4) the retrogression of cordierite and garnet to biotite; (5) the consumption of K-
754 feldspar and the growth of plagioclase; and (6) a decrease in a_{TiO2}. The concurrent breakdown of
755 garnet and growth of zircon, monazite and plagioclase may result in elevated HREE and Y
756 concentrations and more pronounced negative Eu anomalies in newly crystallized accessory
757 minerals. New zircon growth occurs when the a_{TiO2} value of the system ranges from 0.6 to 0.7.
758 Applying the Ti-in-zircon thermometer assuming an a_{TiO2} value of 1.0 would underestimate the
759 true temperature by ~50°C (Fig. 1b). Protracted retrograde monazite and zircon growth is
760 expected during melt crystallization along the isobaric cooling segment of the counterclockwise
761 *P–T* path (e.g., Korhonen et al. 2013b)
762
763 **Greywacke**
764 ***Phase relations***. The pseudosection for the greywacke is shown in Figure 9. When
765 compared with the metapelite, the greywacke composition is less fertile (e.g., Clemens and

766 Vielzeuf 1987; Thompson 1996; Vielzeuf and Schmidt 2001; Johnson et al. 2008; Yakymchuk
767 and Brown 2014a), contains different mineral assemblages, and yields different reaction
768 sequences. For the greywacke, quartz, ilmenite, plagioclase and garnet are stable across the
769 entire diagram. Cordierite becomes stable at pressures of 5–7 kbar with increasing temperature.
770 Orthopyroxene is stable at $P < 6$ kbar and $T > 800$°C. Rutile is stable at $P > 9$–11 kbar.
771 Muscovite is stable at $P > 7$–12 kbar with increasing temperature. Similar to the metapelite,
772 partial melting of the greywacke begins at the wet solidus at temperatures of ~670–700°C. A
773 narrow low-variance field representing the breakdown of muscovite to produce K-feldspar is
774 restricted to $P > 10.8$ kbar; this contrasts with a similar field in the metapelite pseudosection that
775 extends from < 4 to > 12 kbar (Fig. 7). For the greywacke composition, biotite breakdown
776 generates garnet at high pressure, cordierite at low pressure, and orthopyroxene at low pressure
777 and high temperature.
778
779 ***Reaction sequence for the clockwise P–T path***. The mode-box and titania activity for the
780 clockwise assemblage sequence are shown in Figure 10a. The predicted amount of monazite and
781 zircon remaining along with the ASI of melt are shown in Figure 10b. Along the clockwise *P–T*
782 path, partial melting begins at ~675°C at the wet solidus and muscovite is not stable. Therefore,
783 further melting proceeds through the breakdown of biotite and sillimanite to produce garnet.
784 Similar to the metapelite, growing garnet has the potential to capture inherited or prograde
785 monazite and zircon allowing their preservation to higher temperatures. K-feldspar becomes
786 stable at 800°C and 8.2 kbar and biotite is completely consumed by 850°C. Up to this point, the
787 greywacke has produced 14 mol% melt, which is less than the 34 mol% melt generated by the
788 pelite for the same *P–T* path. Up to 850°C, melt is produced gradually for the greywacke

789 composition whereas melting of the metapelite occurs as a pulse in the narrow muscovite–K-
790 feldspar field followed by more gradual melting due to biotite breakdown.

791 Beyond the loss of biotite from the stable assemblage, melting continues through the
792 breakdown of K-feldspar, plagioclase and quartz and an additional 4 mol% melt is produced by
793 900°C. Although monazite dissolution is modelled to continue from 850 to 900°C, some
794 prograde monazite crystallization may be possible in this temperature range for three reasons.
795 First, the melt is saturated with respect to LREE due to progressive monazite dissolution.
796 Second, after the exhaustion of biotite the melt becomes progressively drier, which decreases the
797 solubility of monazite. Third, melt ASI increases, which increases the dissolution of apatite and
798 may liberate enough LREE to support new monazite growth. However, unless this monazite is
799 sequestered away in a growing peritectic mineral (such as garnet) it is expected to be consumed
800 during further heating and partial melting.

801 All of the monazite and ~65% of the zircon are consumed by 900°C. Isothermal
802 decompression from 9 kbar to 7 kbar produces an additional 4 mol% melt and results in minor
803 (<1 mol%) garnet consumption. Melt ASI increases from 1.18 to 1.23 during decompression,
804 which enhances the solubility of apatite. However, the melt is undersaturated with respect to
805 LREE and new monazite growth is not expected during decompression. Approximately 10% of
806 the initial amount of zircon present at the solidus is consumed during decompression and titania
807 activity decreases from 0.95 to 0.85.

808 Cooling and decompression from peak *T* to 750°C results in: (1) melt crystallization, (2)
809 the consumption of garnet and sillimanite to produce cordierite commencing at 890°C and biotite
810 starting at 840°C, (3) a decrease in a_{TiO2} from 0.85 to 0.65, (4) a decrease in melt ASI from 1.23
811 to 1.16, (5) the growth of new zircon (likely as overgrowths on existing zircon), and (6) the

812 crystallization of monazite starting at ~885°C. Zircon and monazite growth occurs during garnet
813 breakdown and these accessory minerals are expected to have elevated Y and HREE
814 concentrations. The application of Ti-in-zircon thermometry should use an a_{TiO2} value ranging
815 from 0.85 to 0.65. Assuming a a_{TiO2} value of 1.0 would underestimate temperatures by up to
816 50°C (Fig. 1b).
817
818 ***Reaction sequence for the counterclockwise P–T path***. The mode-box and titania
819 activity for the counterclockwise assemblage sequence are shown in Figure 10c. The amount of
820 monazite and zircon remaining as well as melt ASI are shown in Figure 10d. Similar to the
821 clockwise *P–T* path for the greywacke, the prograde segment of the counterclockwise *P–T* path
822 generates melt gradually in contrast to the more pulsed melting in the metapelite. Melting
823 commences at the wet solidus and proceeds via the breakdown of biotite to produce cordierite
824 and garnet followed by K-feldspar at 760°C. Orthopyroxene enters the phase assemblage at
825 825°C and biotite is completely consumed by 830°C. The value of a_{TiO2} decreases from ~0.80 to
826 0.60 up to the orthopyroxene-in field boundary and then increases for the remainder of the
827 prograde path. The increase in pressure near peak *T* results in the breakdown of orthopyroxene to
828 produce garnet (e.g., White et al. 2008). By the end of the heating segment, ~50% of the zircon
829 and ~70% of the monazite that was present at the solidus has been consumed. Melt ASI varies
830 between 1.16 and 1.11 during the prograde path. As with the clockwise *P–T* path, melting above
831 the biotite-stability field (in this case from 830–860°C) has the potential to generate some
832 prograde monazite if LREE-rich apatite is consumed. A total of 18 mol% melt is predicted to be
833 generated during heating, which is significantly less than the 44 mol% produced along the same
834 *P–T* path for the metapelite.

Consistent with the metapelite for the same *P–T* path, isobaric cooling results in melt crystallization and monazite and zircon growth. The mode of garnet decreases by 7 mol% and K-feldspar breaks down to sillimanite in the presence of melt at 815°C. Zircon and monazite crystallization is predicted to have elevated Y and HREE due to the breakdown of garnet. Zircon growth occurs when the a_{TiO2} value of the system is ~0.7.

Average Mid Ocean Ridge Basalt

Phase relations. The *P–T* pseudosection for an average MORB composition is shown in Figure 11. The wet solidus has a negative slope from 4 to 11.5 kbar and a positive slope at *T* >11.5 kbar. The temperature of the wet solidus ranges from 620 to 700°C over the modelled *P–T* range. Garnet is stable from 10–14 kbar with decreasing temperature. Orthopyroxene enters the assemblage at temperatures of 800°C to 900°C with increasing *P* and is not stable above 10 kbar at high *T*. Garnet and orthopyroxene are only stable together at pressures of 9.5–10 kbar and at *T* > 900°C. Rutile is stable at *T* > 790°C at *P* > 7 kbar.

Reaction sequence for the clockwise P–T path. The mode-box and titania activity for the reaction sequence as well as the amount of zircon remaining and melt ASI are shown in Figure 12. Melting starts at the wet solidus at 630°C and 9.7 kbar and generates ~ 2 mol% melt and ~ 2 mol% clinopyroxene at the expense of epidote and biotite. A minor amount (~2 mol%) of zircon is expected to be consumed in order to saturate the melt in Zr. Epidote can be an important source of Zr (e.g., Kohn et al. 2015) and the breakdown of Zr-rich epidote may result in Zr saturation and minor zircon crystallization at this stage. After the exhaustion of biotite at ~650°C, melting continues via the breakdown of hornblende, titanite and quartz to produce an

858 additional 4 mol% melt as well as peritectic clinopyroxene by 800°C and 11.4 kbar. During this
859 portion of the prograde path, a_{TiO2} increases from 0.6 at the wet solidus up to 0.9 at 800°C. The
860 amount of zircon remaining is ~80 mol% of the amount present at the solidus. Melt ASI
861 increases slightly from 0.99 to 1.00.

862 Garnet becomes stable at ~800°C and melting proceeds through the breakdown of
863 hornblende and titanite. Garnet growth may include zircon grains that would be isolated from the
864 reacting volume of the rock and zircon could be preserved to higher *T*. Rutile becomes stable at
865 818°C and titanite is completely consumed by 821°C. The peak pressure of 12 kbar is reached at
866 850°C and at this point the system contains ~13 mol% melt, 10 mol% garnet and 65% of the
867 zircon has been consumed. Although zircon is expected to be consumed during partial melting,
868 the breakdown of Zr-rich amphibole (e.g., Sláma et al. 2007) may yield enough Zr to
869 oversaturate the melt and grow new zircon; this zircon may be relatively depleted in HREE in
870 response to the presence of garnet in the rock.

871 The isobaric heating segment of the *P–T* path at peak *P* produces garnet at the expense of
872 hornblende and quartz. Quartz is exhausted at 905°C. This has implications for applying the Ti-
873 in-zircon thermometer, which uses a_{SiO2} as a variable. Zircon is completely consumed by 880°C
874 and the melt produced at higher *T* is expected to be undersaturated in Zr. A consequence of this
875 is that prograde zircon growth at $T > 880$°C is unlikely because any excess Zr due to the
876 breakdown of other minerals (e.g., amphibole) will be incorporated into the Zr-undersaturated
877 melt. At the metamorphic peak of 950°C, the system contains ~28 mol% melt, ~20 mol% garnet
878 and ~14% hornblende.

879 Isothermal decompression from 12 to 10 kbar results in significant garnet consumption
880 (from 20 to 9 mol%), hornblende growth (from 14 to 24 mol%) and minor melt consumption

881 (from 28 to 27 mol%). Zirconium liberated from garnet breakdown is expected to be partitioned
882 between the Zr-undersaturated melt and hornblende. Consequently, zircon crystallization is
883 unlikely. Orthopyroxene enters the assemblage at 10.1 kbar and grows at the expense of garnet,
884 which is exhausted by 9.7 kbar. If garnet is completely consumed, any liberated zircon may
885 become available to the reacting volume and will likely be consumed into the Zr-undersaturated
886 melt. Rutile is completely consumed by 9.1 kbar and a_{TiO2} decreases with further decompression.
887 At the end of the isothermal decompression segment of the *P–T* path the amount of
888 orthopyroxene reaches 5 mol%. No new zircon growth is expected during the isothermal
889 decompression segment because: (1) there is a <1 mol% melt change during isothermal
890 decompression and the melt is already significantly undersaturated in Zr, (2) the *M* value of the
891 melt (cation ratio of [Na + K + 2Ca]/ [Al x Si]) increases from 1.6 to 1.7, which results in an
892 increases the Zr required to saturate the melt (Harrison and Watson 1983; Boehnke et al. 2013),
893 (3) the mode of hornblende increases from 14 to 23 mol%, likely accommodating significant
894 amounts of Zr at high temperature (e.g., Kohn et al. 2015).
895 Cooling and decompression from 950°C at 8 kbar to 800°C at 6 kbar results in the
896 consumption of 17 mol% melt and the complete breakdown of orthopyroxene by ~830°C.
897 Zirconium saturation of the melt is reached at ~870°C and zircon begins to crystallize. At
898 ~850°C, approximately 20% of the amount of zircon originally present at the solidus has grown
899 back and this zircon expected to be enriched in HREE because there is no garnet present in the
900 system. Zircon growth at this stage occurs in a system with an a_{TiO2} value of 0.9 and in the
901 absence of quartz, which is important for the application of Ti-in-zircon thermometry.
902
903 **Summary of reaction sequence modelling**

Linking the trace element concentrations of accessory minerals to the key major minerals (e.g., garnet and plagioclase) requires an understanding of the reaction sequences for a particular bulk composition. Key minerals like garnet and plagioclase can grow or be consumed multiple times along a *P–T* path during heating and cooling or burial and exhumation (Figs 3–10). For example, garnet is predicted to grow in the subsolidus greywacke composition during heating and burial and garnet breakdown occurs during cooling and exhumation for the hairpin *P–T* path (Fig. 6b). By contrast, garnet growth and consumption occurs multiple times along the heating and increasing pressure segment of the *P–T* paths for the subsolidus metapelite composition (Fig. 4). Therefore, high-Y and high-HREE zones in monazite that can be linked to garnet breakdown may reflect the burial and/or exhumation portions of a *P–T* path.

Titania activity also varies along the modelled *P–T* paths and this needs to be taken into account when applying Ti-in-zircon or Ti-in-quartz thermometers. In general, new zircon growth in subsolidus rocks is expected to be limited because major minerals such as hornblende and garnet can accommodate more Zr with increasing temperature. One exception to this may be minor zircon growth through the breakdown of Zr-rich epidote. For the suprasolidus *P–T* paths for the metapelite and greywacke, new zircon growth is expected during cooling and melt crystallization; this growth is predicted to occur when bulk rock a_{TiO2} is less than one for all of the modelled *P–T* paths. If the Ti-in-zircon thermometer is applied with an a_{TiO2} value of one, then the result will be an underestimation in peak metamorphic temperatures by up to ~40°C. For the MORB composition, new zircon growth occurs at $a_{TiO2} < 1.0$ as cooling and melt crystallization occurs outside the stability field of rutile (Fig. 12).

In suprasolidus metamorphic rocks, zircon and monazite are expected to be consumed along the prograde path and new growth is generally predicted to occur along the cooling path.

927 Zircon and monazite dissolution is non-linear and the rate increases with increasing temperature.
928 For the clockwise *P–T* path for the metapelite and greywacke, an increase in the melt ASI leads
929 to more apatite dissolution. Because the melt is saturated in LREE with respect to monazite up to
930 820°C, apatite breakdown may liberate enough LREE to promote new monazite growth.
931 However, after the exhaustion of monazite, the melt is expected to be undersaturated in LREE
932 and prograde monazite growth at the expense of LREE-rich apatite is unlikely. For the
933 counterclockwise *P–T* path for the metapelite and greywacke, melt ASI increases and decreases
934 during the *P–T* evolution and monazite growth from apatite breakdown will be more complex to
935 interpret.
936 The metapelite is expected to lose most of the inherited or subsolidus prograde monazite
937 and zircon during heating above the solidus (unless these mineral are sequestered away from the
938 reaction volume) whereas a larger proportion of these minerals remains in the greywacke
939 composition except for the clockwise *P–T* path where monazite is completely consumed for the
940 greywacke. The difference reflects the fertility of the two rocks; pelites generate more melt than
941 the greywacke and require more Zr and LREE to saturate this melt. Therefore, less fertile
942 compositions, such as greywackes, are more likely to preserve subsolidus zircon and monazite.
943
944 **COMPLICATING FACTORS**
945 **Changes in effective bulk composition**
946 Phase equilibria modelling requires an assessment of the effective bulk composition of a
947 system that is used to model the *P–T* phase relations for a rock (e.g., Stüwe 1997). The effective
948 bulk composition approximates the composition ‘available’ to the rock in which equilibrated
949 mineral assemblages and reaction sequence develop. In natural systems, the effective bulk

composition may change along a *P–T* path (e.g., Guevara and Caddick 2016), which has subsequent implications for modelling reaction sequences in both subsolidus and suprasolidus metamorphic rocks. There are two main mechanisms that can change the effective bulk composition of a metamorphic system: fractionation of elements into growing porphyroblasts and melt loss.

Growing porphyroblasts can fractionate certain elements into their cores that become unavailable to the reacting system in the remainder of the rock. For example, chemical zoning in garnet is commonly preserved in metamorphic rocks because cation diffusion in garnet is relatively slow (e.g., Chakraborty and Ganguly 1992). The preferential partitioning of elements into garnet cores reduces their effective composition in the reactive volume of the rock (e.g., Lanari and Engi, 2017). Some of the consequences for using phase diagrams to infer metamorphic conditions considering garnet fractionation include reduced stability fields for garnet (Gaides et al. 2008) and other minerals (Zuluaga et al. 2005; Moynihan and Pattison 2013) as well as changes in mineral compositional isopleths for garnet (Evans 2004; Gaides et al. 2006) and plagioclase (Moynihan and Pattison 2013). While crystal fractionation needs to be assessed on a case-by-case basis, it is generally most important to consider for greenschist- and amphibolite-facies metamorphic assemblages where mineral chemistries are particularity useful for determining *P–T* conditions. At higher grades, the use of mineral composition isopleths is generally less effective due to retrograde exchange reactions (e.g., Spear and Florence 1992; Kohn and Spear 2000; Pattison et al. 2003). For zircon, the fractionation of Zr into growing garnet (e.g., Kohn et al. 2015) may reduce the Zr budget available for zircon growth.

In high-grade metamorphic rocks that underwent anatexis the preservation of peritectic minerals and lack of extensive retrogression supports melt drainage during prograde

973 metamorphism (Fyfe 1973; Powell 1983; White and Powell 2002; Guernina and Sawyer 2003;
974 Reno et al. 2012). Melt loss produces progressively more refractory bulk compositions, which
975 results in elevated solidus temperatures in the residual rocks. In migmatites that have undergone
976 melt loss, suprasolidus zircon and monazite growth is generally expected to occur during cooling
977 from peak *T* to the elevated solidus (e.g., Kelsey et al. 2008; Spear and Pyle 2010; Yakymchuk
978 and Brown 2014b). Therefore, rocks that have experienced identical *P–T* histories but variable
979 amounts of melt loss and have different solidus temperatures should record a range of ages (e.g.,
980 Korhonen et al. 2013b).
981
982 **Bulk composition and the suprasolidus behaviour of zircon and monazite**
983 For the modelled suprasolidus reaction sequences, the preservation of subsolidus (e.g.,
984 prograde or inherited) zircon and monazite is mainly related to the fertility of the rocks. The
985 metapelite generates more melt along the same *P–T* path than the greywacke. Consequently,
986 zircon and monazite are completely consumed for the metapelite composition along both *P–T*
987 paths (Figs 8a, b) whereas some zircon and/or monazite can survive in the greywacke. An
988 additional factor is the bulk rock content of Zr for zircon and LREE and phosphorus for monazite
989 (e.g., Kelsey et al. 2008; Yakymchuk and Brown 2014b). Both of these factors are explored
990 together in Figure 13.
991 The temperature–composition diagrams in Figure 13 illustrate the variation in melt mode
992 and the stability of zircon and monazite for compositions ranging linearly from the metapelite
993 (left side) to that of the greywacke (right side). The diagrams are isobaric and were calculated at
994 7 kbar because this pressure intersects the main melt producing reactions for both bulk
995 compositions. The common reaction to both compositions is the breakdown of biotite to produce

996 cordierite at ~840–845°C (Fig. 13a). The amount of melt in the metapelite composition is
997 roughly twice the amount in the greywacke composition over the range of modelled temperatures
998 (Fig. 13b). For a bulk composition of 150 ppm Zr, zircon is completely consumed in the
999 metapelite composition by 925°C whereas only 30% of the zircon has been consumed in the
1000 greywacke composition at the same temperature (Fig. 13c). For a bulk composition of 150 ppm
1001 LREE, monazite is completely consumed by 830°C for the metapelite and 880°C for the
1002 greywacke (Fig. 13d). The slopes of the dissolution contours are steeper for zircon than for
1003 monazite in Figures 13c and 13d. This indicates that zircon dissolution is more sensitive to bulk
1004 composition (metapelite vs. greywacke) than monazite.
1005 The sensitivity of zircon and monazite dissolution to bulk composition of Zr and LREE is
1006 explored in Figures 13e and 13f. The contours represent the complete dissolution of zircon and
1007 monazite for various bulk rock Zr and LREE contents. For low-Zr pelites with concentrations of
1008 50 ppm, zircon is completely consumed by 860°C, which is 65°C lower than for a closer-to-
1009 average Zr concentration of 150 ppm. Greywackes with low concentrations of Zr (e.g., 50 ppm)
1010 can still preserve zircon up to UHT conditions due to their lower fertility. Monazite dissolution
1011 contours in Figure 13f have shallower slopes than those for zircon (Fig. 13e), which again
1012 suggests that monazite dissolution is less sensitive to bulk composition. A metapelite with low
1013 concentrations of LREE (e.g., 50 ppm) is predicted to lose monazite by 780°C and monazite is
1014 expected to be completely consumed in the greywacke composition by 820°C. Preserving
1015 subsolidus monazite to UHT conditions requires very LREE-rich compositions of >400 ppm for
1016 the metapelite and >180 ppm for the greywacke. Therefore, a strategy for finding subsolidus
1017 prograde zircon and monazite in migmatites is to choose samples with the highest concentrations
1018 of Zr and LREE.

1019 The breakdown of LREE-rich apatite is a potential mechanism to promote prograde
1020 suprasolidus monazite growth (e.g., Johnson et al. 2015). This is most likely to occur when the
1021 anatectic melt is saturated with respect to monazite in LREE. After the exhaustion of monazite,
1022 the melt is expected to be undersaturated and LREE liberated from the breakdown of apatite is
1023 not predicted to generate new prograde monazite growth. In principle, the higher the bulk rock
1024 LREE the longer monazite will persist during a suprasolidus heating path and the longer the melt
1025 will remain saturated with respect to LREE (Fig. 13f). A further consideration is that bulk
1026 compositions with low phosphorus concentrations may lose apatite during the prograde path and
1027 would result in melt that is undersaturated in P. This may promote further monazite dissolution
1028 instead of monazite growth. Therefore, LREE and P-rich bulk compositions should be targeted
1029 for accessory mineral geochronology to constrain the timing of suprasolidus prograde monazite
1030 growth.
1031
1032 **Effects of open system behaviour on accessory minerals**
1033 Dissolution/re-precipitation of accessory minerals in metamorphic rocks due to the
1034 infiltration of an externally derived fluid has been documented in experiments and studies of
1035 natural samples (e.g., Tomaschek et al. 2003; Crowley et al. 2008; Harlov and Hetherington
1036 2010; Blereau et al. 2016). The careful integration of petrography with the chemistries of these
1037 minerals can be used to provide information on the timing of fluid infiltration (e.g., Williams et
1038 al. 2011) and on fluid chemistry (e.g., Harlov et al. 2011; Taylor et al. 2014; Shazia et al. 2015).
1039 However, the timing of fluid ingress relative to the metamorphic history and the chemistry of
1040 these fluids are highly variable and should to be assessed on a case-by-case basis.

For migmatites that have lost melt, the extraction of melt saturated in Zr or LREE will also change the effective composition of the residuum (e.g., Rapp et al. 1987), which has subsequent consequences for zircon and monazite dissolution. For example, consider the muscovite to K-feldspar melting reaction for the metapelite along the clockwise *P*–*T* path at ~730°C and 7.5 kbar and consider bulk rock values of 150 ppm for LREE and Zr. This reaction involves a large positive volume change (e.g., Powell et al. 2005), which may be accommodated by melt extraction from the rock. When muscovite is exhausted the rock contains ~9 mol% melt. The saturation concentrations of LREE and Zr in the melt at this point are 195 ppm and 137 ppm, respectively. Assuming 8 vol% melt (approximately equivalent to 8 mol%) is extracted (leaving 1 vol% in the rock along grain boundaries), mass balance can be used to determine the amount of Zr and LREE left in the system. For this example, the effective concentration of LREE in the rock decreases to 146 ppm and the effective concentration of Zr increases to 151 ppm. Although the changes to the bulk composition are minor in this example, monazite is predicted to be completely consumed at lower *T* and zircon may persist to higher *T* than for closed system (Fig. 13). For rocks with very low concentrations of Zr and LREE, melt extraction can have a more significant impact on the effective bulk concentrations of these elements and the stability of zircon and monazite (e.g., Yakymchuk and Brown 2014b).

Inclusion/host relationships

An important consideration for accessory mineral reactivity is their inclusion in the major rock-forming minerals (Watson et al. 1989; Bea et al. 2006). Watson et al. (1989) showed that for a Himalayan migmatite sample roughly 78% of the zircon mass is located along grain boundaries and the remaining 28% is included in major minerals (predominately biotite and

garnet), though how representative this is of typical migmatitic gneiss is unknown. Consequently, the breakdown of major minerals may liberate accessory minerals into the reacting volume of the rock that would otherwise be sequestered away.

Inclusions of zircon and monazite that are isolated from the reaction volume may also reduce the effective bulk rock concentration of Zr and LREE (Yakymchuk and Brown 2014b). For example, consider a bulk rock composition of LREE with half of the monazite sequestered away from the reaction volume as inclusions. For a metapelite with a bulk rock LREE composition of 300 ppm and considering that half of this is unavailable, the effective concentration of LREE is 150 ppm. The complete dissolution of monazite is modelled to occur at 830°C in contrast to 870°C for the scenario where all monazite is available for reaction (Fig. 13f). Therefore, applying the models in Figure 13 to natural examples requires an estimate of the amount of zircon or monazite sequestered away from the reaction volume as inclusions as well as an estimate of the amount of Zr and LREE locked away in the major minerals.

The heterogeneous distribution of melt and minerals in high-grade metamorphic rocks also has implications for the dissolution and preservation of accessory minerals. Even for an initially homogenous protolith, *in situ* melt may be spatially associated with peritectic minerals in isolated patches; this produces a heterogeneous melt framework (e.g., White et al. 2004). Zircon and monazite proximal to the zones of incipient melting and in chemical communication with this melt are more likely to contribute to Zr and LREE saturation of the melt whereas more distal grains may not. Consequently, detrital, inherited or prograde (subsolidus or early suprasolidus) zircon and monazite are more likely to be preserved in domains away from incipient melting whereas post-peak and retrograde zircon and monazite may be spatially associated with *in situ* leucosome.

CONCLUDING REMARKS

One important facet of petrochronology is to link the ages of accessory mineral chronometers to the *P–T* information obtained from major rock-forming minerals in metamorphic rocks. The growth and consumption of major minerals is important because these minerals: (1) may contain the necessary essential structural constituents to promote accessory mineral growth directly from their breakdown, (2) are repositories of the trace elements used to link accessory mineral chronometers to *P–T* conditions (e.g., Sr and Eu related to stability of plagioclase as well as Y and HREE reflecting the growth/consumption of garnet), (3) are important hosts for accessory mineral inclusions, and (4) play a role in controlling the component activities (e.g., a_{TiO2}) along a *P–T* evolution. The main controls on accessory mineral behaviour differ between subsolidus and suprasolidus metamorphic conditions.

For subsolidus metamorphism, zircon is generally unreactive and monazite can grow during the prograde and retrograde segments. Linking ages from these accessory mineral to a metamorphic history requires an understanding of the major mineral reaction sequence as well as the behaviour of accessory minerals like xenotime, apatite and allanite. Major minerals such as garnet or plagioclase may experience growth and breakdown stages at any point along a *P–T* path: linking their behaviour to the trace element chemistries of accessory minerals requires an assessment of the reaction sequence for a particular rock along a well-constrained *P–T* path.

For suprasolidus metamorphism, phase equilibria modelling predicts that both zircon and monazite will be consumed during prograde metamorphism and grow during cooling and melt crystallization. However, this contrasts with some studies that have convincingly showed evidence for suprasolidus prograde zircon and monazite growth. For monazite, apatite

dissolution may have contributed to minor prograde monazite growth if the anatectic melt is saturated in LREE. For zircon, solid-state breakdown of major minerals that contain appreciable quantities of Zr may facilitate prograde zircon growth. Ostwald ripening may also play a role in the prograde growth of both zircon and monazite, but this mechanism is still incompletely understood.

Acknowledgements

We thank Mark Caddick and Dave Waters for thorough and perceptive reviews and Pierre Lanari for his patient editorial work. Nonetheless, the authors are responsible for any misinterpretations or omissions that persist. CY was partially funded by a National Sciences and Engineering Research Council of Canada Discovery Grant.

References

Ague JJ (1991) Evidence for major mass transfer and volume strain during regional metamorphism of pelites. Geology 19:855–858

Ashley KT, Law RD (2015) Modeling prograde TiO2 activity and its significance for Ti-in-quartz thermobarometry of pelitic metamorphic rocks. Contr Mineral and Petrol 169:1–7

Ayers JC, Miller C, Gorisch B, Milleman J (1999) Textural development of monazite during high-grade metamorphism: Hydrothermal growth kinetics, with implications for U, Th-Pb geochronology. Am Mineral 84:1766–1780

Baxter EF, Scherer EE (2013) Garnet geochronology: timekeeper of tectonometamorphic processes. Elements 9:433–438

Baxter EF (2017) Title of Chapter. Rev Mineral Geochem XX:xxx–xxx.

Bea F, Pereira MD, Stroh A (1994) Mineral/leucosome trace-element partitioning in a peraluminous migmatite (a laser ablation-ICP-MS study). Chem Geol 117:291–312

Bea F, Montero P (1999) Behavior of accessory phases and redistribution of Zr, REE, Y, Th, and U during metamorphism and partial melting of metapelites in the lower crust: an example from the Kinzigite Formation of Ivrea-Verbano, NW Italy. Geochim Cosmochim Acta 63:1133-1153

Bea F, Montero P, Ortega M (2006) A LA–ICP–MS evaluation of Zr reservoirs in common crustal rocks: implications for Zr and Hf geochemistry, and zircon-forming processes. Can Mineral 44:693–714

Berman RG (1988) Internally-consistent thermodynamic data for minerals in the system Na2O-K2O-CaO-MgO-FeO-Fe2O3-Al2O3-SiO2-TiO2-H2O-CO2. J Petrol 29:445–522

1145 Bingen B, Austrheim H, Whitehouse M (2001) Ilmenite as a source for zirconium during high-
1146 grade metamorphism? Textural evidence from the Caledonides of Western Norway and
1147 implications for zircon geochronology. J Petrol 42:355–375
1148 Blereau E, Clark C, Taylor RJM, Johnson TJ, Fitzsimons I, Santosh M (2016) Constraints on the
1149 timing and conditions of high-grade metamorphism, charnockite formation and fluid‐
1150 rock interaction in the Trivandrum Block, southern India. J Metamorph Geol 34:527–549.
1151 Boehnke P, Watson EB, Trail D, Harrison TM, Schmitt AK (2013) Zircon saturation re-revisited.
1152 Chem Geol 351:324–334
1153 Brown M (1998) Unpairing metamorphic belts: P–T paths and a tectonic model for the Ryoke
1154 Belt, southwest Japan. J Metamorph Geol 16:3–22
1155 Brown M (2014) The contribution of metamorphic petrology to understanding lithosphere
1156 evolution and geodynamics. Geosci Front 5:553–569
1157 Brown M, Kothonen FJ (2009) Some remarks on melting and extreme metamorphism of crustal
1158 rocks. *In*: Physics and Chemistry of the Earth's Interior. Gupta AK and Dasgupta S (eds)
1159 Springer, p 67–87
1160 Caddick MJ, Kohn MJ (2013) Garnet: Witness to the evolution of destructive plate boundaries.
1161 Elements 9:427–432
1162 Carlson WD (1999) The case against Ostwald ripening of porphyroblasts. Can Mineral 37:403–
1163 414
1164 Carlson WD (2000) The case against Ostwald ripening of porphyroblasts: reply. Can Mineral
1165 38:1029–1031
1166 Catlos EJ, Harrison TM, Kohn MJ, Grove M, Ryerson FJ, Manning CE, Upreti BN (2001)
1167 Geochronologic and thermobarometric constraints on the evolution of the Main Central
1168 Thrust, central Nepal Himalaya. J Geophys Res B: Solid Earth 106:16177–16204
1169 Chakraborty S, Ganguly J (1992) Cation diffusion in aluminosilicate garnets: experimental
1170 determination in spessartine-almandine diffusion couples, evaluation of effective binary
1171 diffusion coefficients, and applications. Contr Mineral and Petrol 111:74–86
1172 Chambers JA, Kohn MJ (2012) Titanium in muscovite, biotite, and hornblende: Modeling,
1173 thermometry, and rutile activities of metapelites and amphibolites. Am Mineral 97:543–
1174 555
1175 Chen Y-X, Zheng Y-F, Hu Z (2013) Synexhumation anatexis of ultrahigh-pressure metamorphic
1176 rocks: petrological evidence from granitic gneiss in the Sulu orogen. Lithos 156:69–96
1177 Clark C, Fitzsimons ICW, Healy D, Harley SL (2011) How does the continental crust get really
1178 hot? Elements 7:235–240
1179 Clark C, Kirkland CL, Spaggiari CV, Oorschot C, Wingate MTD, Taylor RJ (2014) Proterozoic
1180 granulite formation driven by mafic magmatism: An example from the Fraser Range
1181 Metamorphics, Western Australia. Precambrian Res 240:1–21
1182 Clark DJ, Hensen BJ, Kinny PD (2000) Geochronological constraints for a two-stage history of
1183 the Albany–Fraser Orogen, Western Australia. Precambrian Res 102:155-183
1184 Clarke GL, Guiraud M, Powell R, Burg JP (1987) Metamorphism in the Olary Block, South
1185 Australia: compression with cooling in a Proterozoic fold belt. J Metamorph Geol 5:291–
1186 306
1187 Clemens JD, Vielzeuf D (1987) Constraints on melting and magma production in the crust. Earth
1188 Planet Sci Lett 86:287–306

1189 Collins WJ, Vernon RH (1991) Orogeny associated with anticlockwise PTt paths: Evidence from
1190 low-P, high-T metamorphic terranes in the Arunta inlier, central Australia. Geology
1191 19:835–838
1192 Connolly JAD, Petrini K (2002) An automated strategy for calculation of phase diagram sections
1193 and retrieval of rock properties as a function of physical conditions. J Metamorph Geol
1194 20:697–708
1195 Copeland RA, Frey FA, Wones DR (1971) Origin of clay minerals in a Mid-Atlantic Ridge
1196 sediment. Earth Planet Sci Lett 10:186–192
1197 Corrie SL, Kohn MJ (2008) Trace-element distributions in silicates during prograde
1198 metamorphic reactions: Implications for monazite formation. J Metamorph Geol 26:451–
1199 464
1200 Crowley JL, Brown RL, Gervais F, Gibson HD (2008) Assessing inheritance of zircon and
1201 monazite in granitic rocks from the Monashee Complex, Canadian Cordillera. J Petrol
1202 49:1915–1929
1203 Crowley JL, Waters DJ, Searle MP, Bowring SA (2009) Pleistocene melting and rapid
1204 exhumation of the Nanga Parbat massif, Pakistan: Age and P–T conditions of accessory
1205 mineral growth in migmatite and leucogranite. Earth Planet Sci Lett 288:408–420
1206 Dawson GC, Krapež B, Fletcher IR, McNaughton NJ, Rasmussen B (2003) 1.2 Ga thermal
1207 metamorphism in the Albany–Fraser Orogen of Western Australia: consequence of
1208 collision or regional heating by dyke swarms? J Geol Soc London 160:29–37
1209 de Capitani C, Brown TH (1987) The computation of chemical equilibrium in complex systems
1210 containing non-ideal solutions. Geochim Cosmochim Acta 51:2639–2652
1211 de Capitani C, Petrakakis K (2010) The computation of equilibrium assemblage diagrams with
1212 Theriak/Domino software. Am Mineral 95:1006–1016
1213 Degeling H, Eggins S, Ellis DJ (2001) Zr budgets for metamorphic reactions, and the formation
1214 of zircon from garnet breakdown. Mineral Mag 65:749–758
1215 Diener JFA, Powell R (2010) Influence of ferric iron on the stability of mineral assemblages. J
1216 Metamorph Geol 28:599–613
1217 Dragovic B, Baxter EF, Caddick MJ (2015) Pulsed dehydration and garnet growth during
1218 subduction revealed by zoned garnet geochronology and thermodynamic modeling,
1219 Sifnos, Greece. Earth Planet Sci Lett 413:111-122
1220 Dragovic B, Samanta LM, Baxter EF, Selverstone J (2012) Using garnet to constrain the
1221 duration and rate of water-releasing metamorphic reactions during subduction: an
1222 example from Sifnos, Greece. Chem Geol 314:9–22
1223 Dragovic B, Guevara VE, Caddick MJ, Baxter EF, Kylander-Clark ARC (2016) A pulse of
1224 cryptic granulite-facies metamorphism in the Archean Wyoming Craton revealed by Sm–
1225 Nd garnet and U–Pb monazite geochronology. Precambrian Res 283:24–49
1226 Duc-Tin Q, Keppler H (2015) Monazite and xenotime solubility in granitic melts and the origin
1227 of the lanthanide tetrad effect. Contr Mineral and Petrol 169:1–26
1228 Enami M, Liou JG, Mattinson CG (2004) Epidote minerals in high P/T metamorphic terranes:
1229 Subduction zone and high-to ultrahigh-pressure metamorphism. Rev Mineral Geochem
1230 56:347–398
1231 Engi (2017) Title of Chapter. Rev Mineral Geochem XX:xxx–xxx.
1232 England PC, Thompson AB (1984) Pressure—Temperature—Time Paths of Regional
1233 Metamorphism I. Heat Transfer during the Evolution of Regions of Thickened
1234 Continental Crust. J Petrol 25:894–928

1235 Evans TP (2004) A method for calculating effective bulk composition modification due to
1236 crystal fractionation in garnet-bearing schist: implications for isopleth thermobarometry.
1237 J Metamorph Geol 22:547–557
1238 Ewing TA, Rubatto D, Hermann J (2014) Hafnium isotopes and Zr/Hf of rutile and zircon from
1239 lower crustal metapelites (Ivrea–Verbano Zone, Italy): implications for chemical
1240 differentiation of the crust. Earth Planet Sci Lett 389:106-118
1241 Ferry JM, Watson EB (2007) New thermodynamic models and revised calibrations for the Ti-in-
1242 zircon and Zr-in-rutile thermometers. Contr Mineral and Petrol 154:429–437
1243 Finger F, Krenn E (2007) Three metamorphic monazite generations in a high-pressure rock from
1244 the Bohemian Massif and the potentially important role of apatite in stimulating
1245 polyphase monazite growth along a PT loop. Lithos 95:103–115
1246 Finger F, Krenn E, Schulz B, Harlov D, Schiller D (2016) “Satellite monazites” in
1247 polymetamorphic basement rocks of the Alps: Their origin and petrological significance.
1248 Am Mineral 101:1094–1103
1249 Fitzsimons IC, Kinny PD, Wetherley S, Hollingsworth DA (2005) Bulk chemical control on
1250 metamorphic monazite growth in pelitic schists and implications for U–Pb age data. J
1251 Metamorph Geol 23:261–277
1252 Florence FP, Spear FS (1993) Influences of reaction history and chemical diffusion on PT
1253 calculations for staurolite schists from the Littleton Formation, northwestern New
1254 Hampshire. Am Mineral 78:345–359
1255 Foster G, Kinny P, Vance D, Prince C, Harris N (2000) The significance of monazite U–Th–Pb
1256 age data in metamorphic assemblages; a combined study of monazite and garnet
1257 chronometry. Earth Planet Sci Lett 181:327–340
1258 Foster G, Gibson H, Parrish RR, Horstwood MSA, Fraser J, Tindle A (2002) Textural, chemical
1259 and isotopic insights into the nature and behaviour of metamorphic monazite. Chem Geol
1260 191:183–207
1261 Foster G, Parrish RR, Horstwood MS, Chenery S, Pyle J, Gibson HD (2004) The generation of
1262 prograde P–T–t points and paths; a textural, compositional, and chronological study of
1263 metamorphic monazite. Earth Planet Sci Lett 228:125–142
1264 Franz G, Andrehs G, Rhede D (1996) Crystal chemistry of monazite and xenotime from
1265 Saxothuringian-Moldanubian metapelites, NE Bavaria, Germany. European Journal of
1266 Mineralogy:1097-1118
1267 Franz G, Morteani G, Rhede D (2015) Xenotime-(Y) formation from zircon dissolution–
1268 precipitation and HREE fractionation: an example from a metamorphosed phosphatic
1269 sandstone, Espinhaço fold belt (Brazil). Contr Mineral and Petrol 170:1–22
1270 Fraser G, Ellis D, Eggins S (1997) Zirconium abundance in granulite-facies minerals, with
1271 implications for zircon geochronology in high-grade rocks. Geology 25:607–610
1272 Frei D, Liebscher A, Franz G, Dulski P (2004) Trace element geochemistry of epidote minerals.
1273 Rev Mineral Geochem 56:553–605
1274 Frost BR, Chamberlain KR, Schumacher JC (2001) Sphene (titanite): phase relations and role as
1275 a geochronometer. Chem Geol 172:131–148
1276 Fyfe WS (1973) The granulite facies, partial melting and the Archaean crust. Philos Trans R Soc
1277 London, Ser A 273:457–461
1278 Gaidies F, Abart R, De Capitani C, Schuster R, Connolly JAD, Reusser E (2006)
1279 Characterization of polymetamorphism in the Austroalpine basement east of the Tauern
1280 Window using garnet isopleth thermobarometry. J Metamorph Geol 24:451–475

1281 Gaidies F, De Capitani C, Abart R (2008) THERIA_G: a software program to numerically model
1282 prograde garnet growth. Contr Mineral and Petrol 155:657–671
1283 Gaidies F, Pattison DRM, De Capitani C (2011) Toward a quantitative model of metamorphic
1284 nucleation and growth. Contr Mineral and Petrol 162:975–993
1285 Gasser D, Bruand E, Rubatto D, Stüwe K (2012) The behaviour of monazite from greenschist
1286 facies phyllites to anatectic gneisses: an example from the Chugach Metamorphic
1287 Complex, southern Alaska. Lithos 134:108–122
1288 Gervasoni F, Klemme S, Rocha-Júnior ERV, Berndt J (2016) Zircon saturation in silicate melts:
1289 a new and improved model for aluminous and alkaline melts. Contr Mineral and Petrol
1290 171:1–12
1291 Ghent ED (1976) Plagioclase-garnet-Al_2SiO_5-quartz: a potential geobarometer-geothermometer.
1292 Am Mineral 6:710–714
1293 Gibson HD, Carr SD, Brown RL, Hamilton MA (2004) Correlations between chemical and age
1294 domains in monazite, and metamorphic reactions involving major pelitic phases: an
1295 integration of ID-TIMS and SHRIMP geochronology with Y–Th–U X-ray mapping.
1296 Chem Geol 211:237–260
1297 Grapes RH, Hoskin PWO (2004) Epidote group minerals in low–medium pressure metamorphic
1298 terranes. Rev Mineral Geochem 56:301–345
1299 Green ECR, White RW, Diener JFA, Powell R, Palin RM (2016) Activity–composition relations
1300 for the calculation of partial melting equilibria in metabasic rocks. J Metamorph Geol,
1301 doi: 10.1111/jmg.12211
1302 Gromet LP, Silver LT (1983) Rare earth element distributions among minerals in a granodiorite
1303 and their petrogenetic implications. Geochim Cosmochim Acta 47:925-939
1304 Guernina S, Sawyer EW (2003) Large-scale melt-depletion in granulite terranes: An example
1305 from the Archean Ashuanipi Subprovince of Quebec. J Metamorph Geol 21:181–201
1306 Guevara VE, Caddick MJ (2016) Shooting at a moving target: phase equilibria modelling of
1307 high-temperature metamorphism. J Metamorph Geol 34:209–235.
1308 Hacker BR, Andersen TB, Johnston S, Kylander-Clark ARC, Peterman EM, Walsh EO, Young
1309 D (2010) High-temperature deformation during continental-margin subduction &
1310 exhumation: The ultrahigh-pressure Western Gneiss Region of Norway. Tectonophysics
1311 480:149–171
1312 Hacker BR, Kylander-Clark ARC, Holder R, Andersen TB, Peterman EM, Walsh EO,
1313 Munnikhuis JK (2015) Monazite response to ultrahigh-pressure subduction from U–Pb
1314 dating by laser ablation split stream. Chem Geol 409:28–41
1315 Harlov DE, Hetherington CJ (2010) Letter. Partial high-grade alteration of monazite using alkali-
1316 bearing fluids: Experiment and nature. Am Mineral 95:1105–1108
1317 Harlov DE, Wirth R, Förster H-J (2005) An experimental study of dissolution–reprecipitation in
1318 fluorapatite: fluid infiltration and the formation of monazite. Contr Mineral and Petrol
1319 150:268–286
1320 Harlov DE, Wirth R, Hetherington CJ (2011) Fluid-mediated partial alteration in monazite: the
1321 role of coupled dissolution–reprecipitation in element redistribution and mass transfer.
1322 Contr Mineral and Petrol 162:329–348
1323 Harris NBW, Caddick M, Kosler J, Goswami S, Vance D, Tindle AG (2004) The pressure–
1324 temperature–time path of migmatites from the Sikkim Himalaya. J Metamorph Geol
1325 22:249–264

1326 Harrison TM, Watson EB (1983) Kinetics of zircon dissolution and zirconium diffusion in
1327 granitic melts of variable water content. Contr Mineral and Petrol 84:66–72
1328 Harrison TM, Watson EB (1984) The behavior of apatite during crustal anatexis: equilibrium and
1329 kinetic considerations. Geochim Cosmochim Acta 48:1467–1477
1330 Hay DC, Dempster TJ (2009) Zircon behaviour during low-temperature metamorphism. J Petrol
1331 50: 571–589.
1332 Hayden LA, Watson EB, Wark DA (2008) A thermobarometer for sphene (titanite). Contr
1333 Mineral and Petrol 155:529–540
1334 Hensen BJ (1971) Theoretical phase relations involving cordierite and garnet in the system
1335 MgO-FeO-Al2O3-SiO2. Contr Mineral and Petrol 33:191-214
1336 Hermann J, Rubatto D (2003) Relating zircon and monazite domains to garnet growth zones: age
1337 and duration of granulite facies metamorphism in the Val Malenco lower crust. J
1338 Metamorph Geol 21:833-852
1339 Hermann J, Rubatto D, Korsakov A, Shatsky VS (2001) Multiple zircon growth during fast
1340 exhumation of diamondiferous, deeply subducted continental crust (Kokchetav Massif,
1341 Kazakhstan). Contr Mineral and Petrol 141:66–82
1342 Hiess J, Nutman AP, Bennett VC, Holden P (2008) Ti-in-zircon thermometry applied to
1343 contrasting Archean metamorphic and igneous systems. Chem Geol 247:323–338
1344 Hofmann AE, Baker MB, Eiler JM (2013) An experimental study of Ti and Zr partitioning
1345 among zircon, rutile, and granitic melt. Contr Mineral and Petrol 166:235–253
1346 Holder RM, Hacker BR, Kylander-Clark ARC, Cottle JM (2015) Monazite trace-element and
1347 isotopic signatures of (ultra) high-pressure metamorphism: Examples from the Western
1348 Gneiss Region, Norway. Chem Geol 409:99–111
1349 Holland TJB, Powell R (1998) An internally consistent thermodynamic data set for phases of
1350 petrological interest. J Metamorph Geol 16:309–343
1351 Holland TJB, Powell R (2011) An improved and extended internally consistent thermodynamic
1352 dataset for phases of petrological interest, involving a new equation of state for solids. J
1353 Metamorph Geol 29:333–383
1354 Hoskin PWO, Schaltegger U (2003) The composition of zircon and igneous and metamorphic
1355 petrogenesis. Rev Mineral Geochem 53:27–62
1356 Huang WL, Wyllie PJ (1973) Melting relations of muscovite-granite to 35 kbar as a model for
1357 fusion of metamorphosed subducted oceanic sediments. Contr Mineral and Petrol 42:1-14
1358 Jamieson RA, Beaumont C, Medvedev S, Nguyen MH (2004) Crustal channel flows: 2.
1359 Numerical models with implications for metamorphism in the Himalayan-Tibetan
1360 orogen. J Geophys Res B: Solid Earth 109:2156–2202
1361 Janots E, Engi M, Berger A, Allaz J, Schwarz JO, Spandler C (2008) Prograde metamorphic
1362 sequence of REE minerals in pelitic rocks of the Central Alps: implications for allanite–
1363 monazite–xenotime phase relations from 250 to 610 C. J Metamorph Geol 26:509–526
1364 Janots E, Engi M, Rubatto D, Berger A, Gregory C, Rahn M (2009) Metamorphic rates in
1365 collisional orogeny from in situ allanite and monazite dating. Geology 37:11-14
1366 Johnson TE, White RW, Powell R (2008) Partial melting of metagreywacke: a calculated
1367 mineral equilibria study. J Metamorph Geol 26:837-853
1368 Johnson TE, Clark C, Taylor RJM, Santosh M, Collins AS (2015) Prograde and retrograde
1369 growth of monazite in migmatites: An example from the Nagercoil Block, southern India.
1370 Geosci Front 6:373–387

Kapp P, Manning CE, Tropper P (2009) Phase-equilibrium constraints on titanite and rutile activities in mafic epidote amphibolites and geobarometry using titanite-rutile equilibria. J Metamorph Geol 27:509–521

Kawakami T, Yamaguchi I, Miyake A, Shibata T, Maki K, Yokoyama TD, Hirata T (2013) Behavior of zircon in the upper-amphibolite to granulite facies schist/migmatite transition, Ryoke metamorphic belt, SW Japan: constraints from the melt inclusions in zircon. Contr Mineral and Petrol 165:575–591

Kelsey DE, Powell R (2011) Progress in linking accessory mineral growth and breakdown to major mineral evolution in metamorphic rocks: a thermodynamic approach in the Na2O-CaO-K2O-FeO-MgO-Al2O3-SiO2-H2O-TiO2-ZrO2 system. J Metamorph Geol 29:151–166

Kelsey DE, Hand M (2015) On ultrahigh temperature crustal metamorphism: phase equilibria, trace element thermometry, bulk composition, heat sources, timescales and tectonic settings. Geosci Front 6:311–356

Kelsey DE, Clark C, Hand M (2008) Thermobarometric modelling of zircon and monazite growth in melt-bearing systems: examples using model metapelitic and metapsammitic granulites. J Metamorph Geol 26:199–212

Kingsbury JA, Miller CF, Wooden JL, Harrison TM (1993) Monazite paragenesis and U-Pb systematics in rocks of the eastern Mojave Desert, California, USA: implications for thermochronometry. Chem Geol 110:147–167

Kirkland CL, Spaggiari CV, Johnson TE, Smithies RH, Danišík M, Evans N, Wingate MTD, Clark C, Spencer C, Mikucki E, McDonald BJ (2016) Grain size matters: Implications for element and isotopic mobility in titanite. Precambrian Res 278:283–302

Kohn MJ (2008) PTt data from central Nepal support critical taper and repudiate large-scale channel flow of the Greater Himalayan Sequence. Geol Soc Am Bull 120:259–273

Kohn MJ, Spear F (2000) Retrograde net transfer reaction insurance for pressure-temperature estimates. Geology 28:1127–1130

Kohn MJ, Malloy MA (2004) Formation of monazite via prograde metamorphic reactions among common silicates: implications for age determinations. Geochim Cosmochim Acta 68:101–113

Kohn MJ, Corrie SL, Markley C (2015) The fall and rise of metamorphic zircon. Am Mineral 100:897–908

Kohn (2017) Title of Chapter. Rev Mineral Geochem XX:xxx–xxx.

Korhonen F,J Brown M, Clark C, Bhattacharya S (2013a) Osumilite–melt interactions in ultrahigh temperature granulites: phase equilibria modelling and implications for the P–T–t evolution of the Eastern Ghats Province, India. J Metamorph Geol 31:881–907

Korhonen FJ, Clark C, Brown M, Bhattacharya S, Taylor R (2013b) How long-lived is ultrahigh temperature (UHT) metamorphism? Constraints from zircon and monazite geochronology in the Eastern Ghats orogenic belt, India. Precambrian Res 234:322–350

Korhonen FJ, Clark C, Brown M, Taylor RJM (2014) Taking the temperature of Earth's hottest crust. Earth Planet Sci Lett 408:341–354

Korhonen FJ, Brown M, Grove M, Siddoway CS, Baxter EF, Inglis JD (2012) Separating metamorphic events in the Fosdick migmatite–granite complex, West Antarctica. J Metamorph Geol 30:165–192

Kylander-Clark ARC, Hacker BR, Cottle JM (2013) Laser-ablation split-stream ICP petrochronology. Chem Geol 345:99–112

Lanari and Engi (2017) Title of Chapter. Rev Mineral Geochem XX:xxx–xxx.
Mahar EM, Baker JM, Powell R, Holland TJB, Howell N (1997) The effect of Mn on mineral stability in metapelites. J Metamorph Geol 15:223–238
Mayne MJ, Moyen JF, Stevens G, Kaisl Aniemi L (2016) Rcrust: a tool for calculating path‐dependent open system processes and application to melt loss. J Metamorph Geol 34: 663‐682.
McClelland WC, Lapen TJ (2013) Linking time to the pressure–temperature path for ultrahigh-pressure rocks. Elements 9:273–279
Mezger K, Hanson GN, Bohlen SR (1989) High-precision U–Pb ages of metamorphic rutile: application to the cooling history of high-grade terranes. Earth Planet Sci Lett 96:106-118
Miyazaki K (1991) Ostwald ripening of garnet in high P/T metamorphic rocks. Contr Mineral and Petrol 108:118–128
Miyazaki K (1996) A numerical simulation of textural evolution due to Ostwald ripening in metamorphic rocks: A case for small amount of volume of dispersed crystals. Geochim Cosmochim Acta 60:277–290
Molina JF, Moreno JA, Castro A, Rodríguez C, Fershtater GB (2015) Calcic amphibole thermobarometry in metamorphic and igneous rocks: New calibrations based on plagioclase/amphibole Al-Si partitioning and amphibole/liquid Mg partitioning. Lithos 232:286-305
Montel, J-M Kornprobst, J Vielzeuf, D (2000) Preservation of old U–Th–Pb ages in shielded monazite: example from the Beni Bousera Hercynian kinzigites (Morocco). J Metamorph Geol 18:335–342
Montel J-M (1986) Experimental determination of the solubility of Ce-monazite in SiO2-Al2O3-K2O-Na2O melts at 800 C, 2 kbar, under H2O-saturated conditions. Geology 14:659–662
Morrissey LJ, Hand M, Raimondo T, Kelsey DE (2014) Long-lived high-T, low-P granulite facies metamorphism in the Arunta Region, central Australia. J Metamorph Geol 32:25–47
Moynihan DP, Pattison DRM (2013) An automated method for the calculation of P–T paths from garnet zoning, with application to metapelitic schist from the Kootenay Arc, British Columbia, Canada. J Metamorph Geol 31:525–548
Mulcahy SR, Vervoort JD, Renne PR (2014) Dating subduction-zone metamorphism with combined garnet and lawsonite Lu–Hf geochronology. J Metamorph Geol 32:515–533
Nemchin AA, Bodorkos S (2000) Zr and LREE concentrations in anatectic melt as a function of crystal size distributions of zircon and monazite in the source region. Geological Society of America, Abstracts and Programs: 52286
Nemchin AA, Giannini LM, Bodorkos S, Oliver NHS (2001) Ostwald ripening as a possible mechanism for zircon overgrowth formation during anatexis: theoretical constraints, a numerical model, and its application to pelitic migmatites of the Tickalara Metamorphics, northwestern Australia. Geochim Cosmochim Acta 65:2771–2788
O'Brien PJ, Rötzler J (2003) High-pressure granulites: formation, recovery of peak conditions and implications for tectonics. J Metamorph Geol 21:3–20
Parrish RR (1990) U-Pb dating of monazite and its application to geological problems. Can J Earth Sci 27:1431–1450

1461 Pattison DRM, Tinkham DK (2009) Interplay between equilibrium and kinetics in prograde
1462 metamorphism of pelites: an example from the Nelson aureole, British Columbia. J
1463 Metamorph Geol 27:249–279
1464 Pattison DRM, DeBuhr CL (2015) Petrology of metapelites in the Bugaboo aureole, British
1465 Columbia, Canada. J Metamorph Geol 33:437-462
1466 Pattison DRM, Chacko T, Farquhar J, McFarlane CRM (2003) Temperatures of granulite-facies
1467 metamorphism: constraints from experimental phase equilibria and thermobarometry
1468 corrected for retrograde exchange. J Petrol 44:867–900
1469 Pichavant M, Montel J-M, Richard LR (1992) Apatite solubility in peraluminous liquids:
1470 Experimental data and an extension of the Harrison-Watson model. Geochim Cosmochim
1471 Acta 56:3855-3861
1472 Powell R (1983) Processes in granulite-facies metamorphism. *In*: Proceedings of the
1473 Geochemical Group of the Mineraological Society: Migmatites, melting and
1474 metamorphism. Atherton, MP, Gribble, CD (eds). Shiva, Nantwich, p 127–139
1475 Powell R, Holland TJB (1988) An internally consistent dataset with uncertainties and
1476 correlations: 3. Applications to geobarometry, worked examples and a computer
1477 program. J Metamorph Geol 6:173–204
1478 Powell R, Holland TJB (2008) On thermobarometry. J Metamorph Geol 26:155–179
1479 Powell R, Holland T, Worley B (1998) Calculating phase diagrams involving solid solutions via
1480 non-linear equations, with examples using THERMOCALC. J Metamorph Geol 16:577–
1481 588
1482 Powell R, Guiraud M, White RW (2005) Truth and beauty in metamorphic phase-equilibria:
1483 conjugate variables and phase diagrams. Can Mineral 43:21–33
1484 Pyle JM, Spear FS (1999) Yttrium zoning in garnet: coupling of major and accessory phases
1485 during metamorphic reactions. Geol Mat Res 1:1–49
1486 Pyle JM, Spear FS (2000) An empirical garnet (YAG)–xenotime thermometer. Contr Mineral
1487 and Petrol 138:51–58
1488 Pyle JM, Spear FS, Rudnick RL, McDonough WF (2001) Monazite–xenotime–garnet
1489 equilibrium in metapelites and a new monazite–garnet thermometer. J Petrol 42:2083–
1490 2107
1491 Rapp RP, Watson EB (1986) Monazite solubility and dissolution kinetics: implications for the
1492 thorium and light rare earth chemistry of felsic magmas. Contr Mineral and Petrol
1493 94:304–316
1494 Rapp RP, Ryerson FJ, Miller CF (1987) Experimental evidence bearing on the stability of
1495 monazite during crustal anaatexis. Geophys Res Lett 14:307-310
1496 Rasmussen B (2005) Radiometric dating of sedimentary rocks: the application of diagenetic
1497 xenotime geochronology. Earth Sci Rev 68:197-243
1498 Rasmussen B, Muhling JR (2007) Monazite begets monazite: evidence for dissolution of detrital
1499 monazite and reprecipitation of syntectonic monazite during low-grade regional
1500 metamorphism. Contr Mineral and Petrol 154:675–689
1501 Rasmussen B, Fletcher IR, Muhling JR (2011) Response of xenotime to prograde
1502 metamorphism. Contr Mineral and Petrol 162:1259–1277
1503 Regis D, Warren CJ, Mottram CM, Roberts NMW (2016) Using monazite and zircon
1504 petrochronology to constrain the P–T–t evolution of the middle crust in the Bhutan
1505 Himalaya. J Metamorph Geol

Reno BL, Piccoli PM, Brown M, Trouw RAJ (2012) In situ monazite (U–Th)–Pb ages from the Southern Brasília Belt, Brazil: constraints on the high-temperature retrograde evolution of HP granulites. J Metamorph Geol 30:81–112
Roberts MP, Finger F (1997) Do U-Pb zircon ages from granulites reflect peak metamorphic conditions? Geology 25:319-322
Rocha BC, Moraes R, Möller A, Cioffi CR, Jercinovic MJ (2016) Timing of anatexis and melt crystallization in the Socorro–Guaxupé Nappe, SE Brazil: Insights from trace element composition of zircon, monazite and garnet coupled to U–Pb geochronology. Lithos
Rubatto (2017) Title of Chapter. Rev Mineral Geochem XX:xxx–xxx.
Rubatto D (2002) Zircon trace element geochemistry: partitioning with garnet and the link between U–Pb ages and metamorphism. Chem Geol 184:123–138
Rubatto D, Hermann J (2003) Zircon formation during fluid circulation in eclogites (Monviso, Western Alps): implications for Zr and Hf budget in subduction zones. Geochim Cosmochim Acta 67:2173–2187
Rubatto D, Hermann J (2007) Experimental zircon/melt and zircon/garnet trace element partitioning and implications for the geochronology of crustal rocks. Chem Geol 241:38–61
Rubatto D, Williams IS, Buick IS (2001) Zircon and monazite response to prograde metamorphism in the Reynolds Range, central Australia. Contr Mineral and Petrol 140:458–468
Rubatto D, Chakraborty S, Dasgupta S (2013) Timescales of crustal melting in the Higher Himalayan Crystallines (Sikkim, Eastern Himalaya) inferred from trace element-constrained monazite and zircon chronology. Contr Mineral and Petrol 165:349–372
Schaltegger U (2007) Hydrothermal zircon. Elements 3:51–79
Schaltegger U, Fanning CM, Günther D, Maurin JC, Schulmann K, Gebauer D (1999) Growth, annealing and recrystallization of zircon and preservation of monazite in high-grade metamorphism: conventional and in-situ U-Pb isotope, cathodoluminescence and microchemical evidence. Contr Mineral and Petrol 134:186-201
Sheppard S, Rasmussen B, Muhling JR, Farrell TR, Fletcher IR (2007) Grenvillian-aged orogenesis in the Palaeoproterozoic Gascoyne Complex, Western Australia: 1030‑950 Ma reworking of the Proterozoic Capricorn Orogen. J Metamorph Geol 25:477-494
Shaw DM (1956) Geochemistry of pelitic rocks. Part III: Major elements and general geochemistry. Geol Soc Am Bull 67:919–934
Shazia JR, Harlov DE, Suzuki K, Kim SW, Girish-Kumar M, Hayasaka Y, Ishwar-Kumar C, Windley BF, Sajeev K (2015) Linking monazite geochronology with fluid infiltration and metamorphic histories: Nature and experiment. Lithos 236:1–15
Skora S, Blundy J (2012) Monazite solubility in hydrous silicic melts at high pressure conditions relevant to subduction zone metamorphism. Earth Planet Sci Lett 321:104–114
Sláma J, Košler J, Pedersen RB (2007) Behaviour of zircon in high-grade metamorphic rocks: evidence from Hf isotopes, trace elements and textural studies. Contr Mineral and Petrol 154:335–356
Smith HA, Barreiro B (1990) Monazite U-Pb dating of staurolite grade metamorphism in pelitic schists. Contr Mineral and Petrol 105:602–615
Smye AJ, Stockli DF (2014) Rutile U–Pb age depth profiling: A continuous record of lithospheric thermal evolution. Earth Planet Sci Lett 408:171–182

Spear FS (1995) Metamorphic phase equilibria and pressure-temperature-time paths. Mineralogical Society of America Washington
Spear FS (2010) Monazite–allanite phase relations in metapelites. Chem Geol 279:55-62
Spear FS, Florence FP (1992) Thermobarometry in granulites: pitfalls and new approaches. Precambrian Res 55:209–241
Spear FS, Pyle JM (2002) Apatite, monazite, and xenotime in metamorphic rocks. Rev Mineral Geochem 48:293–335
Spear FS, Pyle JM (2010) Theoretical modeling of monazite growth in a low-Ca metapelite. Chem Geol 273:111–119
Spear FS, Pattison DRM, Cheney JT (2016) The metamorphosis of metamorphic petrology. Geol Soc Am Sp Pap 523:SPE523-502
Spencer KJ, Hacker BR, Kylander-Clark ARC, Andersen TB, Cottle JM, Stearns MA, Poletti JE, Seward GGE (2013) Campaign-style titanite U–Pb dating by laser-ablation ICP: implications for crustal flow, phase transformations and titanite closure. Chem Geol 341:84–101
Stearns MA, Hacker BR, Ratschbacher L, Rutte D, Kylander-Clark ARC (2015) Titanite petrochronology of the Pamir gneiss domes: Implications for middle to deep crust exhumation and titanite closure to Pb and Zr diffusion. Tectonics 34:784–802
Stepanov AS, Hermann J, Rubatto D, Rapp RP (2012) Experimental study of monazite/melt partitioning with implications for the REE, Th and U geochemistry of crustal rocks. Chem Geol 300:200–220
Štípská P, Hacker BR, Racek M, Holder R, Kylander-Clark ARC, Schulmann K, Hasalová P (2015) Monazite Dating of Prograde and Retrograde P–T–d paths in the Barrovian terrane of the Thaya window, Bohemian Massif. J Petrol 56:1007–1035
Stüwe K (1997) Effective bulk composition changes due to cooling: a model predicting complexities in retrograde reaction textures. Contr Mineral and Petrol 129:43–52
Stüwe K, Powell R (1995) PT paths from modal proportions: application to the Koralm Complex, Eastern Alps. Contr Mineral and Petrol 119:83–93
Sun S-S, McDonough W (1989) Chemical and isotopic systematics of oceanic basalts: implications for mantle composition and processes. Geol Soc London, Sp Pub 42:313–345
Suzuki K, Adachi M (1994) Middle Precambrian detrital monazite and zircon from the Hida gneiss on Oki-Dogo Island, Japan: their origin and implications for the correlation of basement gneiss of Southwest Japan and Korea. Tectonophysics 235:277–292
Symmes GH, Ferry JM (1992) The effect of whole-rock MnO content on the stability of garnet in pelitic schists during metamorphism. J Metamorph Geol 10:221–237
Taylor RJM, Clark C, Fitzsimons ICW, Santosh M, Hand M, Evans N, McDonald B (2014) Post-peak, fluid-mediated modification of granulite facies zircon and monazite in the Trivandrum Block, southern India. Contr Mineral and Petrol 168:1–17
Taylor RJM, Harley SL, Hinton RW, Elphick S, Clark C, Kelly NM (2015) Experimental determination of REE partition coefficients between zircon, garnet and melt: a key to understanding high-T crustal processes. J Metamorph Geol 33:231–248
Taylor-Jones K, Powell R (2015) Interpreting zirconium-in-rutile thermometric results. J Metamorph Geol 33:115–122
Thompson AB (1982) Dehydration melting of pelitic rocks and the generation of H_2O-undersaturated granitic liquids. Am J Sci 282:1567–1595

1597 Thompson AB (1996) Fertility of crustal rocks during anatexis. Geol Soc Am Sp Pap 315:1–10
1598 Thompson AB, England PC (1984) Pressure—temperature—time paths of regional
1599 metamorphism II. Their inference and interpretation using mineral assemblages in
1600 metamorphic rocks. J Petrol 25:929–955
1601 Tikare V, Cawley JD (1998) Application of the Potts model to simulation of Ostwald ripening. J
1602 Am Ceram Soc 81:485–491
1603 Tomaschek F, Kennedy AK, Villa IM, Lagos M, Ballhaus C (2003) Zircons from Syros,
1604 Cyclades, Greece—recrystallization and mobilization of zircon during high-pressure
1605 metamorphism. J Petrol 44:1977–2002
1606 Tomkins HS, Powell R, Ellis DJ (2007) The pressure dependence of the zirconium-in-rutile
1607 thermometer. J Metamorph Geol 25:703–713
1608 Vance D, O'Nions RK (1990) Isotopic chronometry of zoned garnets: growth kinetics and
1609 metamorphic histories. Earth Planet Sci Lett 97:227–240
1610 Vance D, Mahar E (1998) Pressure-temperature paths from PT pseudosections and zoned
1611 garnets: potential, limitations and examples from the Zanskar Himalaya, NW India. Contr
1612 Mineral and Petrol 132:225–245
1613 Vavra G, Schmid R, Gebauer D (1999) Internal morphology, habit and U-Th-Pb microanalysis
1614 of amphibolite-to-granulite facies zircons: geochronology of the Ivrea Zone (Southern
1615 Alps). Contr Mineral and Petrol 134:380–404
1616 Vernon RH (1996) Problems with inferring P-T-t paths in low-P granulite facies rocks. J
1617 Metamorph Geol 14:143–153
1618 Vielzeuf D, Schmidt MW (2001) Melting relations in hydrous systems revisited: application to
1619 metapelites, metagreywackes and metabasalts. Contr Mineral and Petrol 141:251–267
1620 Walsh AK, Kelsey DE, Kirkland CL, Hand M, Smithies RH, Clark C, Howard HM (2015) P–T–t
1621 evolution of a large, long-lived, ultrahigh-temperature Grenvillian belt in central
1622 Australia. Gondwana Res 28:531–564
1623 Wark DA, Watson EB (2006) TitaniQ: a titanium-in-quartz geothermometer. Contr Mineral and
1624 Petrol 152:743–754
1625 Warren CJ, Grujic D, Cottle JM, Rogers NW (2012) Constraining cooling histories: rutile and
1626 titanite chronology and diffusion modelling in NW Bhutan. J Metamorph Geol 30:113–
1627 130
1628 Watson EB (1996) Dissolution, growth and survival of zircons during crustal fusion: kinetic
1629 principles, geological models and implications for isotopic inheritance. Geol Soc Am Sp
1630 Pap 315:43–56
1631 Watson EB, Harrison TM (1983) Zircon saturation revisited: temperature and composition
1632 effects in a variety of crustal magma types. Earth Planet Sci Lett 64:295–304
1633 Watson EB, Vicenzi EP, Rapp RP (1989) Inclusion/host relations involving accessory minerals
1634 in high-grade metamorphic and anatectic rocks. Contr Mineral and Petrol 101:220–231
1635 Watson EB, Wark DA, Thomas JB (2006) Crystallization thermometers for zircon and rutile.
1636 Contr Mineral and Petrol 151:413-433
1637 Watt GR, Harley SL (1993) Accessory phase controls on the geochemistry of crustal melts and
1638 restites produced during water-undersaturated partial melting. Contr Mineral and Petrol
1639 114:550–566
1640 White RW, Powell R (2002) Melt loss and the preservation of granulite facies mineral
1641 assemblages. J Metamorph Geol 20:621–632

White RW, Powell R, Halpin JA (2004) Spatially-focussed melt formation in aluminous metapelites from Broken Hill, Australia. J Metamorph Geol 22:825–845
White RW, Pomroy NE, Powell R (2005) An in situ metatexite–diatexite transition in upper amphibolite facies rocks from Broken Hill, Australia. J Metamorph Geol 23:579–602
White RW, Powell R, Johnson TE (2014a) The effect of Mn on mineral stability in metapelites revisited: New a-x relations for manganese-bearing minerals. J Metamorph Geol 32:809–828
White RW, Powell R, Baldwin JA (2008) Calculated phase equilibria involving chemical potentials to investigate the textural evolution of metamorphic rocks. J Metamorph Geol 26:181–198
White RW, Stevens G, Johnson TE (2011) Is the crucible reproducible? Reconciling melting experiments with thermodynamic calculations. Elements 7:241–246
White RW, Powell R, Holland TJB, Johnson TE, Green ECR (2014b) New mineral activity–composition relations for thermodynamic calculations in metapelitic systems. J Metamorph Geol 32:261–286
White WM, Klein EM (2014) 4.13 - Composition of the Oceanic Crust. *In*: Treatise on Geochemsitry (Second Edition). Holland, HD, Turekian, K (ed). Elsevier, Oxford, p 457–496
Williams ML, Jercinovic MJ, Harlov DE, Budzyń B, Hetherington CJ (2011) Resetting monazite ages during fluid-related alteration. Chem Geol 283:218–225
Wing BA, Ferry JM, Harrison TM (2003) Prograde destruction and formation of monazite and allanite during contact and regional metamorphism of pelites: petrology and geochronology. Contr Mineral and Petrol 145:228–250
Wolf MB, London D (1994) Apatite dissolution into peraluminous haplogranitic melts: an experimental study of solubilities and mechanisms. Geochim Cosmochim Acta 58:4127–4145
Wolf MB, London D (1995) Incongruent dissolution of REE-and Sr-rich apatite in peraluminous granitic liquids: Differential apatite, monazite, and xenotime solubilities during anatexis. Am Mineral 80:765–775
Worley B, Powell R (1998) Making movies: phase diagrams changing in pressure, temperature, composition and time. Geol Soc London, Sp Pub 138:269-280
Wu CM (2015) Revised empirical garnet–biotite–muscovite–plagioclase geobarometer in metapelites. J Metamorph Geol 33:167–176
Xu H, Ye K, Song Y, Chen Y, Zhang J, Liu Q, Guo S (2013) Prograde metamorphism, decompressional partial melting and subsequent melt fractional crystallization in the Weihai migmatitic gneisses, Sulu UHP terrane, eastern China. Chem Geol 341:16–37
Yakymchuk C, Brown M (2014a) Consequences of open-system melting in tectonics. J Geol Soc London 171:21–40
Yakymchuk C, Brown M (2014b) Behaviour of zircon and monazite during crustal melting. J Geol Soc London 171:465–479
Yakymchuk C, Brown M, Clark C, Korhonen FJ, Piccoli PM, Siddoway CS, Taylor RJM, Vervoort JD (2015) Decoding polyphase migmatites using geochronology and phase equilibria modelling. J Metamorph Geol 33:203–230
Yardley BWD, Valley JW (1997) The petrologic case for a dry lower crust. J Geophys Res B: Solid Earth 102:12173–12185

Zack T, Moraes R, Kronz A (2004) Temperature dependence of Zr in rutile: empirical calibration of a rutile thermometer. Contr Mineral and Petrol 148:471–488

Zack T, Stockli DF, Luvizotto GL, Barth MG, Belousova E, Wolfe MR, Hinton RW (2011) In situ U–Pb rutile dating by LA-ICP-MS: 208Pb correction and prospects for geological applications. Contr Mineral and Petrol 162:515-530

Zack (2017). Title of Chapter. Rev Mineral Geochem XX:xxx–xxx.

Zuluaga CA, Stowell HH, Tinkham DK (2005) The effect of zoned garnet on metapelite pseudosection topology and calculated metamorphic PT paths. Am Mineral 90:1619–1628

Figure Captions

Figure 1. Underestimation of metamorphic temperature when the bulk rock value of a_{TiO2} is less than 1.0 (the true value is shown by the contours), but a value of 1.0 is assumed in: (a) the Ti-in-quartz thermometer of Wark and Watson (2006), and (b) the Ti-in-zircon thermometer of Ferry and Watson (2007).

Figure 2. Compilation of the range of allanite to monazite reaction temperatures for variable bulk rock pelite compositions. Curves are from Spear (2010).

Figure 3. *P–T* pseudosection for the subsolidus metapelite. The solidus is shown by the heavy dashed line.

Figure 4. (a) Mode-box diagram and a_{TiO2} for the subsolidus clockwise *P–T* path for the metapelite. (b) Mode-box diagram and a_{TiO2} for the subsolidus hairpin *P–T* path.

Figure 5. *P–T* pseudosection for the subsolidus greywacke. The solidus is shown by the heavy dashed line.

Figure 6. (a) Mode-box diagram and a_{TiO2} for the subsolidus clockwise *P–T* path for the greywacke composition. (b) Mode-box diagram and a_{TiO2} for the subsolidus hairpin *P–T* path.

Figure 7. *P–T* pseudosection for suprasolidus metapelite. The solidus is shown by the heavy dashed line.

Figure 8. (a) Mode-box diagram and a_{TiO2} for the suprasolidus clockwise *P–T* path for the metapelite. (b) Amount of zircon and monazite remaining relative to the amount at the solidus and the ASI value of melt. (c) Mode-box diagram and a_{TiO2} for the counterclockwise *P–T* path for the metapelite. (d) Amount of zircon and monazite remaining relative to the amount at the solidus for the counterclockwise *P–T* path.

Figure 9. *P–T* pseudosection for the suprasolidus greywacke. The solidus is shown by the heavy dashed line.

Figure 10. (a) Mode-box diagram and a_{TiO2} for the suprasolidus clockwise *P–T* path for the greywacke. (b) Amount of zircon and monazite remaining relative to the amount at the solidus and the ASI value of melt. (c) Mode-box diagram and a_{TiO2} for the counterclockwise *P–T* path for the greywacke. (d) Amount of zircon and monazite remaining relative to the amount at the solidus for the counterclockwise *P–T* path.

Figure 11. *P–T* pseudosection for the suprasolidus MORB. The solidus is shown by the heavy dashed line.

Figure 12. (a) Mode-box diagram and a_{TiO2} for the suprasolidus clockwise *P–T* path for the MORB. (b) Amount of zircon remaining relative to the amount at the solidus and the ASI value of melt.

Figure 13. (a) *T–X* pseudosection calculated at 7 kbar showing the change in mineral assemblages for compositions ranging from the metapelite (left side) to the greywacke (right side). (b) *T–X* diagram with melt isopleths (mol%). (c) *T–X* diagram with the calculated amount of zircon dissolution assuming a bulk Zr concentration of 150 ppm. (d) Calculated amount of monazite dissolution assuming a bulk LREE concentration of 150 ppm. (e) *T–X* diagram with contours for the complete dissolution of zircon for a range of bulk rock Zr concentrations. (f) *T–X* diagram with contours for the complete dissolution of monazite for a range of bulk rock LREE concentrations.

Table 1. Bulk compositions used for phase equilibria modelling (mol%)

	Figures	**H_2O**	**SiO_2**	**Al_2O_3**	**CaO**	**MgO**	**FeO**	**K_2O**	**Na_2O**	**TiO_2**	**MnO**	**O**
subsolidus												
metapelite	3,4	+	64.58	13.65	1.59	5.53	8.03	2.94	2.00	0.91	0.17	0.60
greywacke	5,6	+	77.62	8.20	1.15	3.85	4.21	1.26	2.85	0.52	0.35	0.32
suprasolidus												
metapelite	7,8,13	6.24	60.55	12.80	1.49	5.18	7.52	2.76	1.88	0.85	0.16	0.60
greywacke	9,10,13	2.61	75.35	7.96	1.12	3.74	4.09	1.22	2.77	0.51	0.34	0.31
MORB	11,12	6.19	42.58	10.45	12.27	14.76	9.68	0.22	2.62	0.66	–	0.58

+ H_2O in excess, – not considered

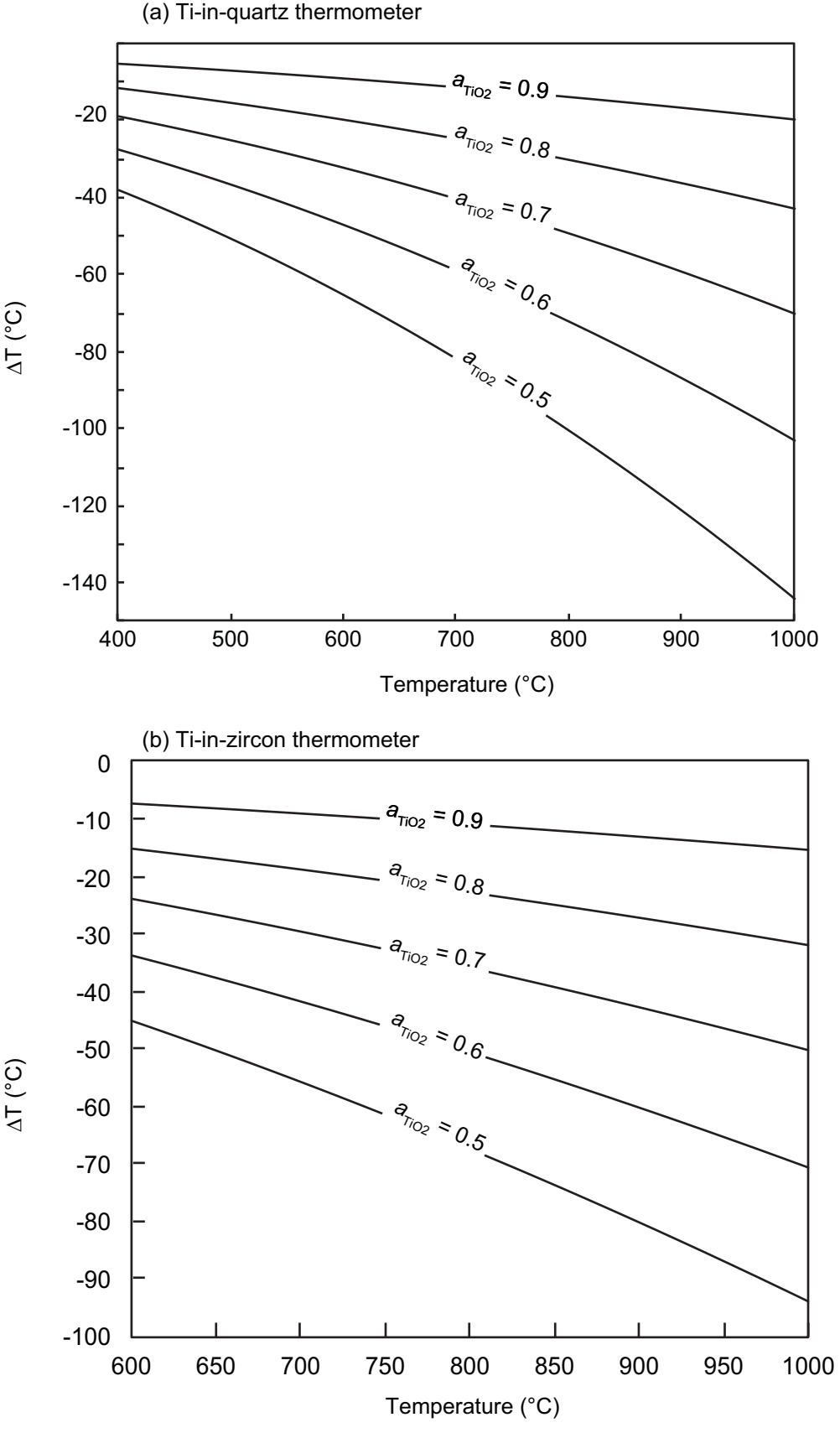
(a) Ti-in-quartz thermometer
a_{TiO2} = 0.9
a_{TiO2} = 0.8
a_{TiO2} = 0.7
a_{TiO2} = 0.6
a_{TiO2} = 0.5
ΔT (°C)
0
-20
-40
-60
-80
-100
-120
-140
400
500
600
700
800
900
1000
Temperature (°C)
(b) Ti-in-zircon thermometer
a_{TiO2} = 0.9
a_{TiO2} = 0.8
a_{TiO2} = 0.7
a_{TiO2} = 0.6
a_{TiO2} = 0.5
ΔT (°C)
0
-10
-20
-30
-40
-50
-60
-70
-80
-90
-100
600
650
700
750
800
850
900
950
1000
Temperature (°C)

Figure 1

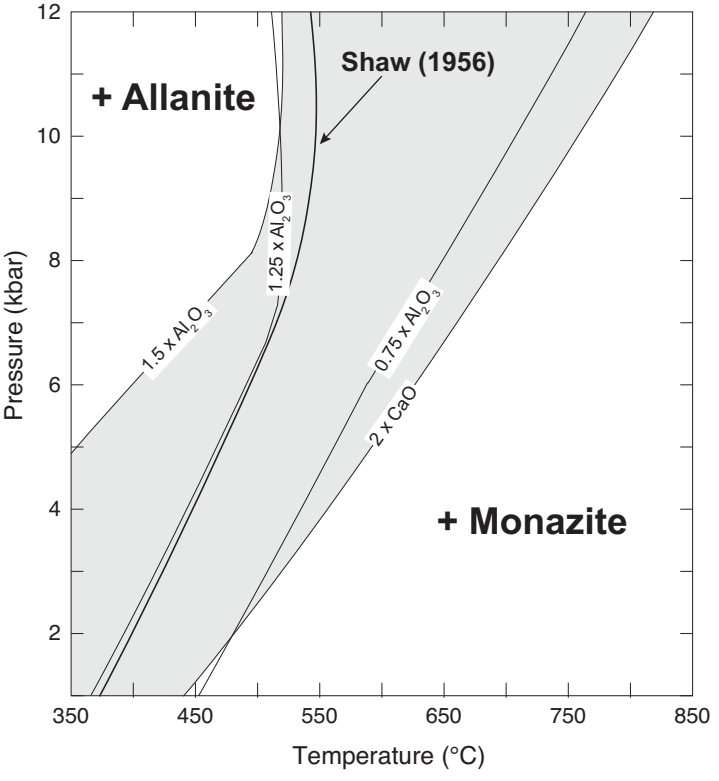
+ Allanite
Shaw (1956)
1.5 x Al2O3
1.25 x Al2O3
0.75 x Al2O3
2 x CaO
+ Monazite
Pressure (kbar)
Temperature (°C)
12
10
8
6
4
2
350
450
550
650
750
850

Figure 2

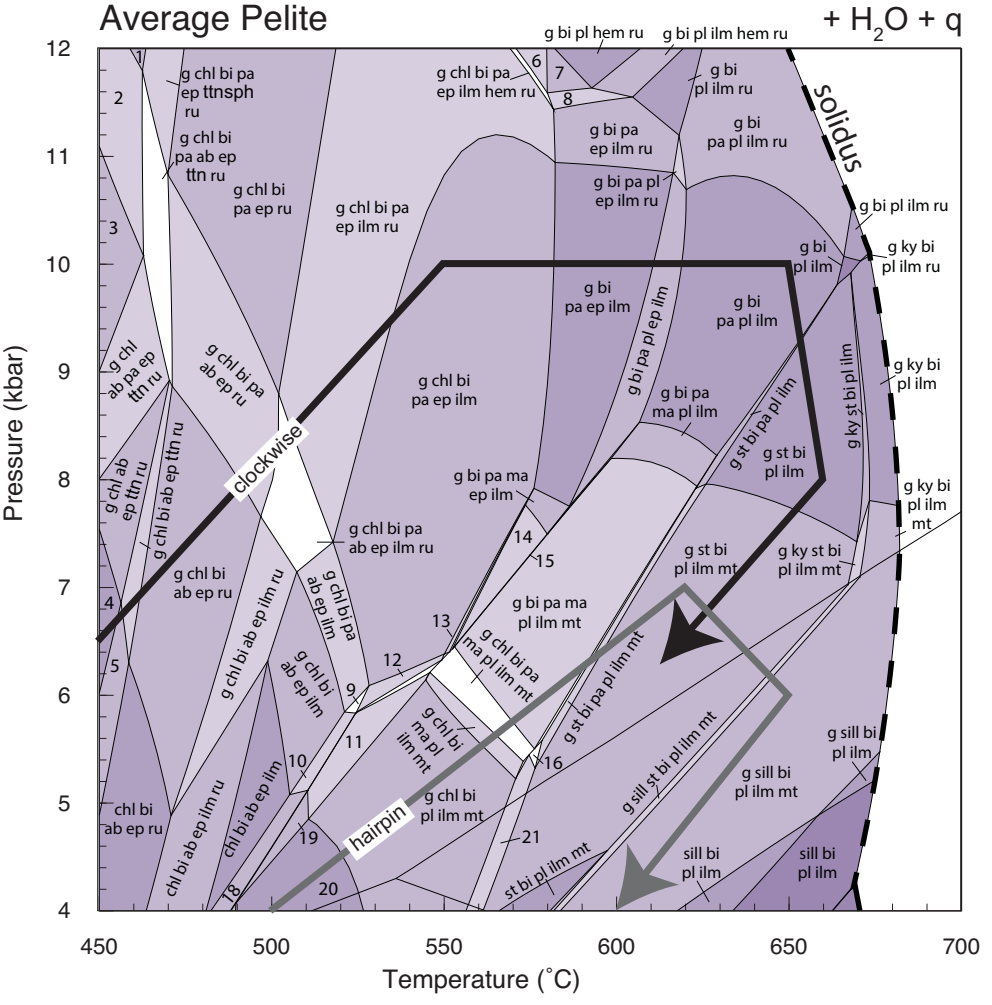

1) g chl bi pa ep ttn
2) g chl bi pa ab ep ttn
3) g chl pa ab ep ttn
4) chl ab ep ttn ru
5) chl bi ab ep ttn ru
6) g chl bi pa ep hem ru
7) g bi pa ep hem ru
8) g bi pa ep ilm hem ru
9) g chl bi pa pl ab ep ilm
10) g chl bi pl ab ep ilm
11) g chl bi pl ep ilm mt
12) g chl bi pa pl ep ilm
13) g chl bi pa ma ep ilm
14) g bi pa ma ep ilm mt
15) g bi pa ma pl ep ilm mt
16) g st chl bi pa pl ilm mt
17) chl bi pl ab ep ilm ru
18) chl bi pl ab ep ilm
19) chl bi pl ep ilm mt
20) chl bi pl ilm mt
21) g st chl bi pl ilm mt

Figure 3

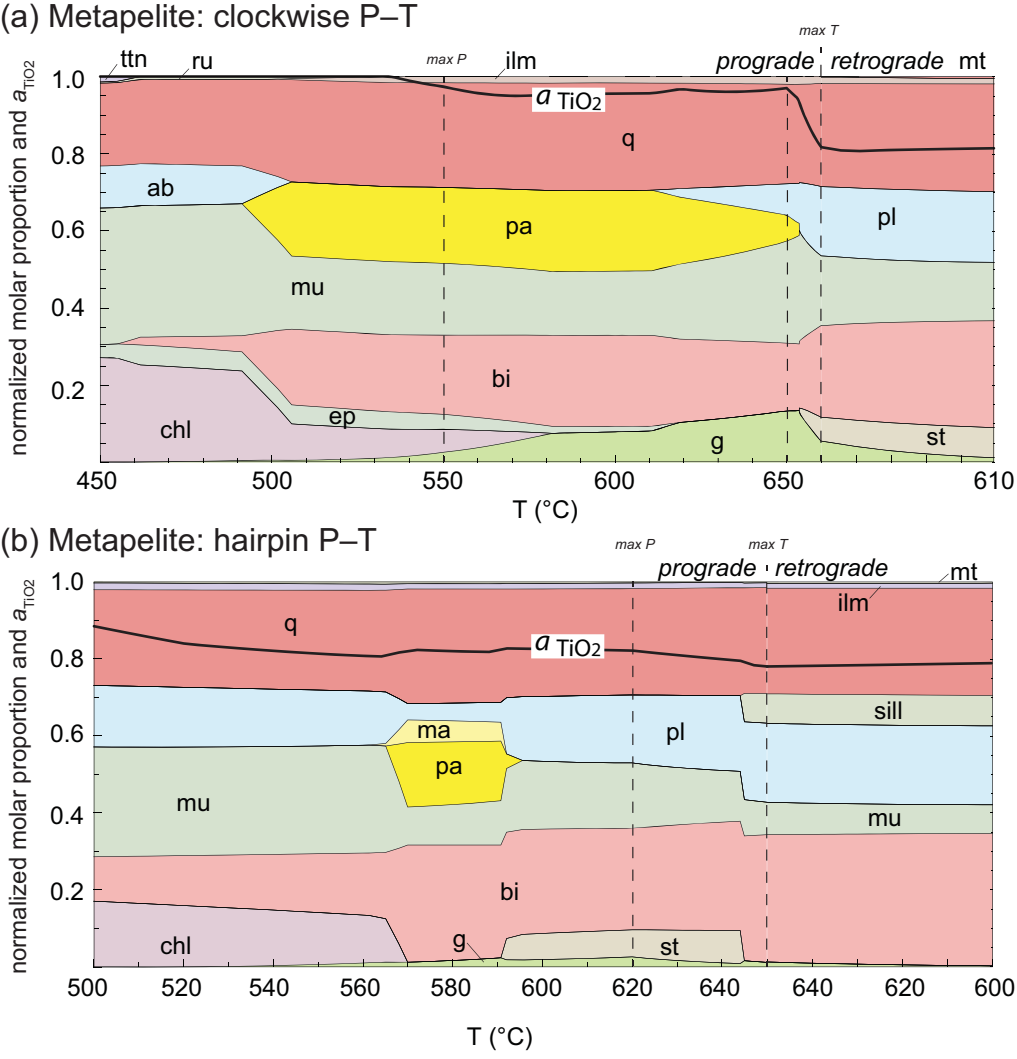
(a) Metapelite: clockwise P–T
max T
ttn
ru
max P
ilm
prograde
retrograde
mt
normalized molar proportion and a_{TiO2}
1.0
0.8
0.6
0.4
0.2
a TiO2
q
ab
pa
pl
mu
bi
ep
chl
g
st
450
500
550
600
650
610
T (°C)
(b) Metapelite: hairpin P–T
max P
max T
prograde
retrograde
mt
ilm
normalized molar proportion and a_{TiO2}
1.0
0.8
0.6
0.4
0.2
q
a TiO2
sill
ma
pa
pl
mu
bi
chl
g
st
500
520
540
560
580
600
620
640
640
620
600
T (°C)

Figure 4.

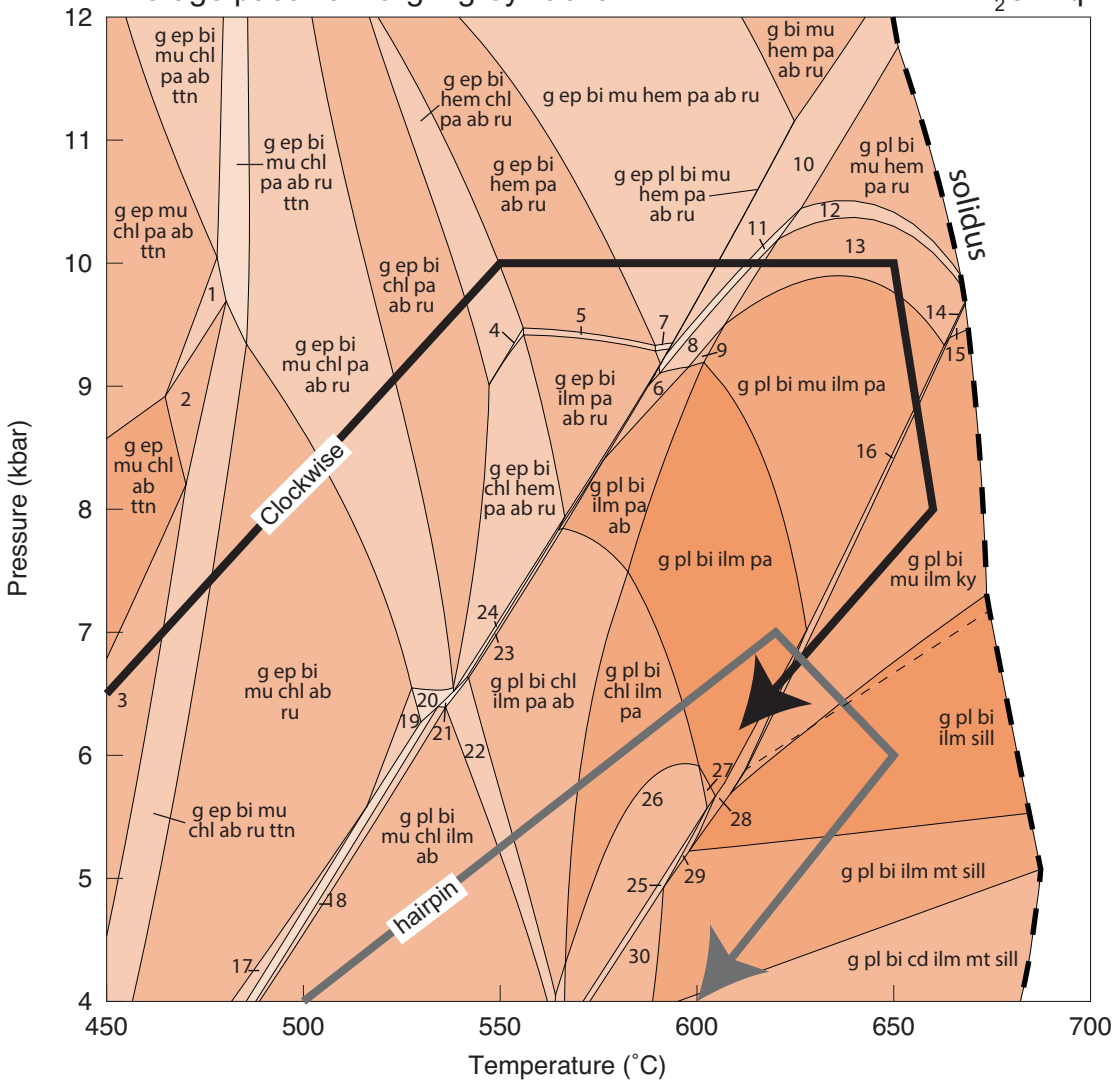

1. g ep mu chl pa ab ru ttn
2. g ep mu chl ab ru ttn
3. g ep bi mu chl ab ttn
4. g ep bi chl ilm hem pa ab ru
5. g ep bi ilm hem pa ab ru
6. g pl bi ilm pa ab ru
7. g ep pl bi mu ilm hem pa ab ru
8. g pl bi mu ilm pa ab ru
9. g pl bi mu ilm pa ab
10. g pl bi mu hem pa ab ru
11. g pl bi mu ilm hem pa ab ru
12. g pl bi mu ilm hem pa ru
13. g pl bi mu ilm pa ru
14. g pl bi mu ilm pa ru ky
15. g pl bi mu ilm ru ky
16. g pl bi mu ilm pa ky
17. g pl ep bi mu chl ab ru
18. g pl ep bi mu chl ilm ab
19. g ep bi mu chl ilm ab ru
20. g ep bi mu chl ilm pa ab ru
21. g pl ep bi mu chl ilm pa ab ru
22. g pl bi mu chl ilm pa ab
23. g pl ep bi chl ilm pa ab
24. g pl ep bi chl ilm pa ab ru
25. g pl bi chl ilm pa mt sill
26. g pl bi chl ilm pa mt
27. g pl bi ilm pa mt
28. g pl bi ilm pa sill
29. g pl bi ilm pa mt sill
30. g pl bi chl ilm mt sill

Figure 5

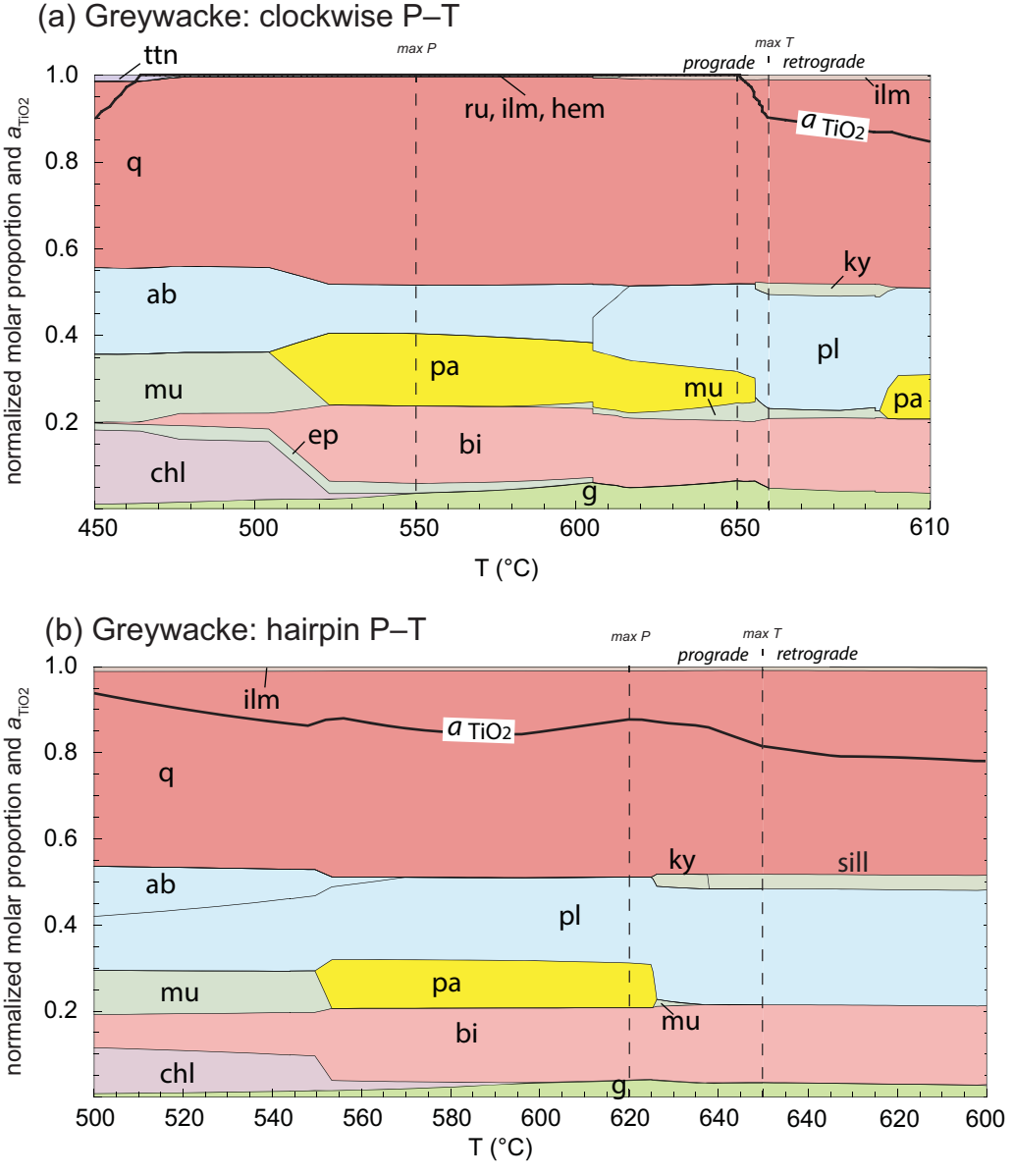
(a) Greywacke: clockwise P–T
ttn
max P
max T
prograde
retrograde
ilm
ru, ilm, hem
a TiO2
q
ky
ab
pl
pa
mu
mu
pa
ep
bi
chl
g
normalized molar proportion and aTiO2
1.0
0.8
0.6
0.4
0.2
450
500
550
600
650
610
T (°C)
(b) Greywacke: hairpin P–T
max P
max T
prograde
retrograde
ilm
a TiO2
q
ky
sill
ab
pl
mu
pa
mu
bi
chl
g
normalized molar proportion and aTiO2
1.0
0.8
0.6
0.4
0.2
500
520
540
560
580
600
620
640
640
620
600
T (°C)

Figure 6

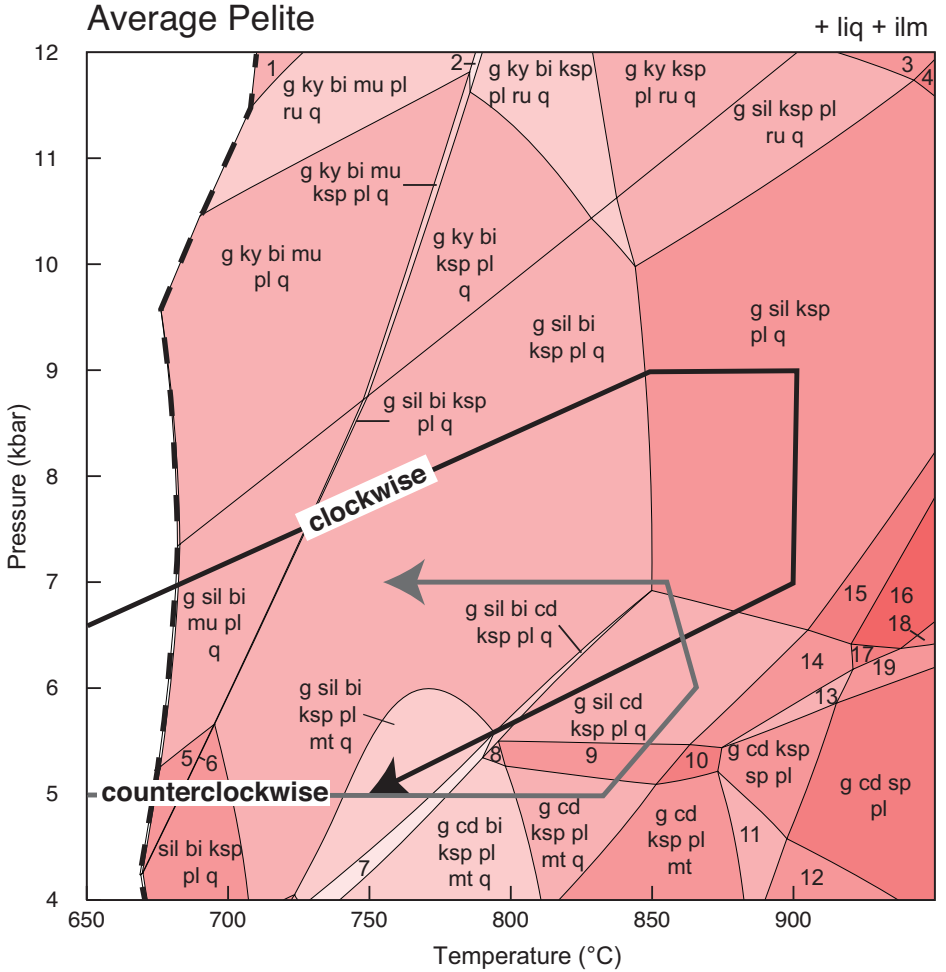

1: g bi bi mu pl ru q
2: g ky bi mu ksp pl ru q
3: g sil ksp ru q
4: g sil ksp q
5: sil bi mu pl q
6: sil ksp bi mu pl q
7: g sil cd bi ksp pl mt q
8: g cd bi ksp pl q
9: g cd ksp pl ru q
10: g cd ksp pl ru
11: g cd ksp sp pl mt
12: g cd sp pl mt
13: g sil cd ksp sp pl
14: g sil cd ksp pl
15: g sil ksp pl
16: g sil pl
17: g sil cd pl
18: g sil sp pl
19: g sil cd sp pl

Figure 7

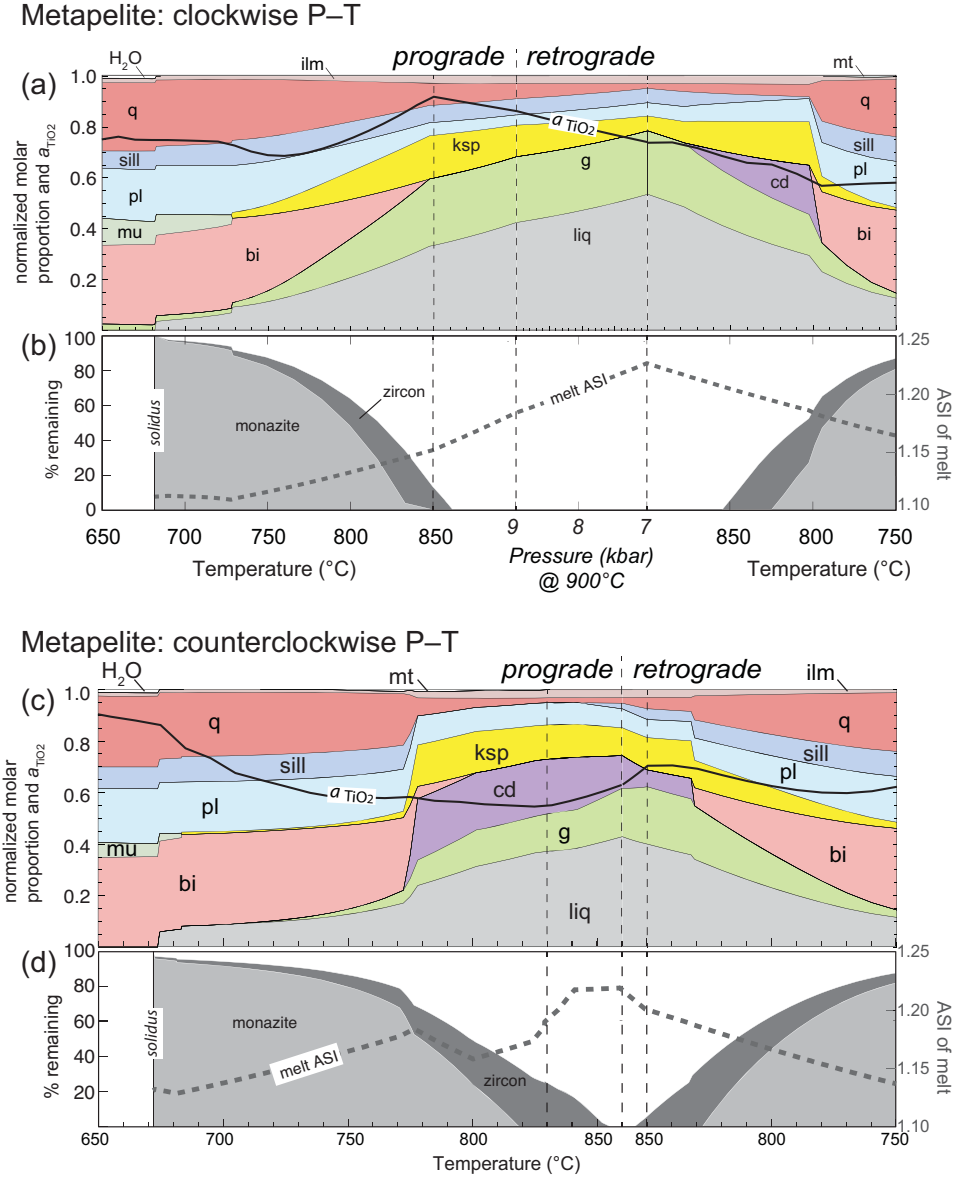
Metapelite: clockwise P–T
(a)
H2O
ilm
prograde
retrograde
mt
normalized molar proportion and aTiO2
q
sill
pl
mu
bi
ksp
g
cd
liq
aTiO2
(b)
% remaining
solidus
monazite
zircon
melt ASI
ASI of melt
Temperature (°C)
Pressure (kbar) @ 900°C
Metapelite: counterclockwise P–T
(c)
(d)

Figure 8

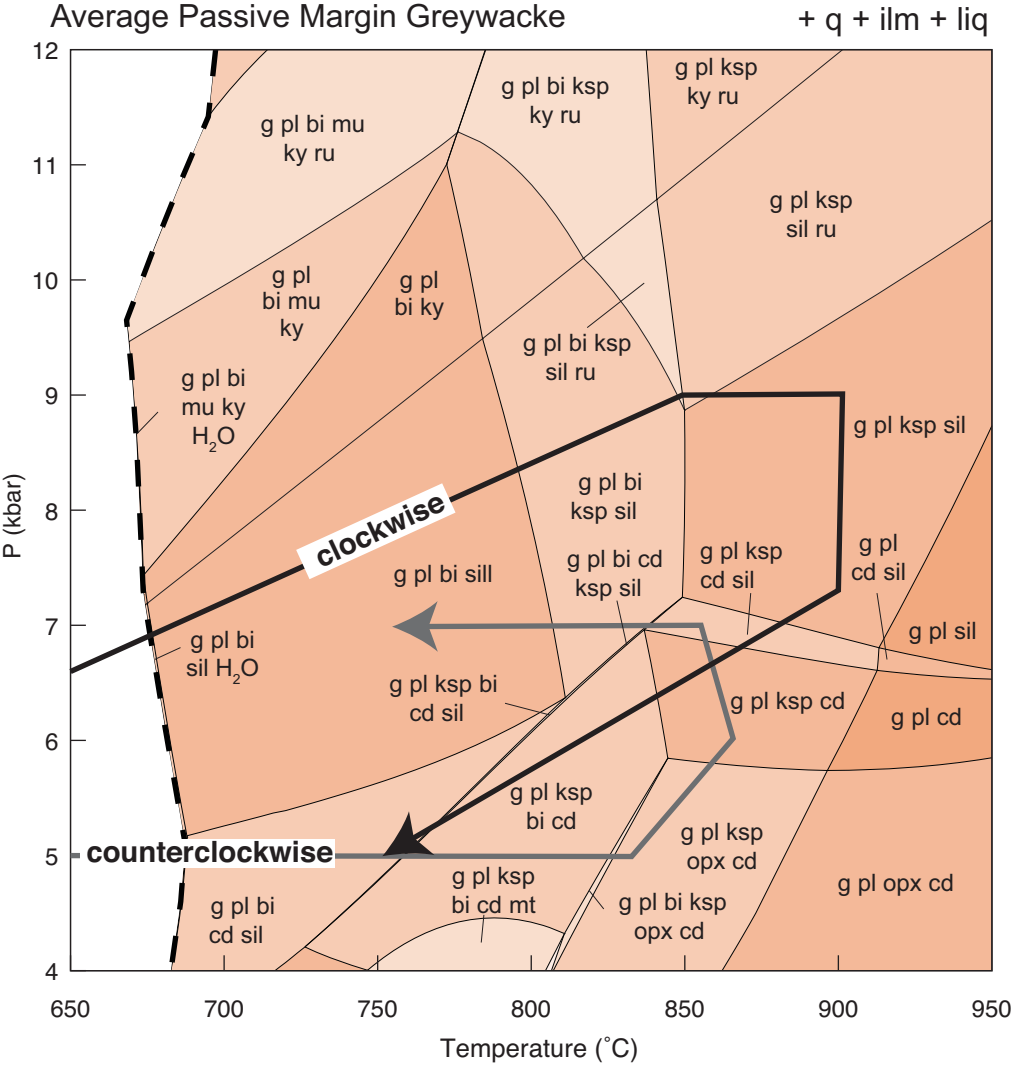
Average Passive Margin Greywacke
+ q + ilm + liq
g pl bi mu ky ru
g pl bi ksp ky ru
g pl ksp ky ru
g pl ksp sil ru
g pl bi mu ky
g pl bi ky
g pl bi ksp sil ru
g pl bi mu ky H2O
g pl ksp sil
g pl bi ksp sil
clockwise
g pl bi sill
g pl bi cd ksp sil
g pl ksp cd sil
g pl cd sil
g pl sil
g pl bi sil H2O
g pl ksp bi cd sil
g pl ksp cd
g pl cd
g pl ksp bi cd
counterclockwise
g pl ksp opx cd
g pl opx cd
g pl bi cd sil
g pl ksp bi cd mt
g pl bi ksp opx cd
P (kbar)
Temperature (˚C)
12
11
10
9
8
7
6
5
4
650
700
750
800
850
900
950

Figure 9

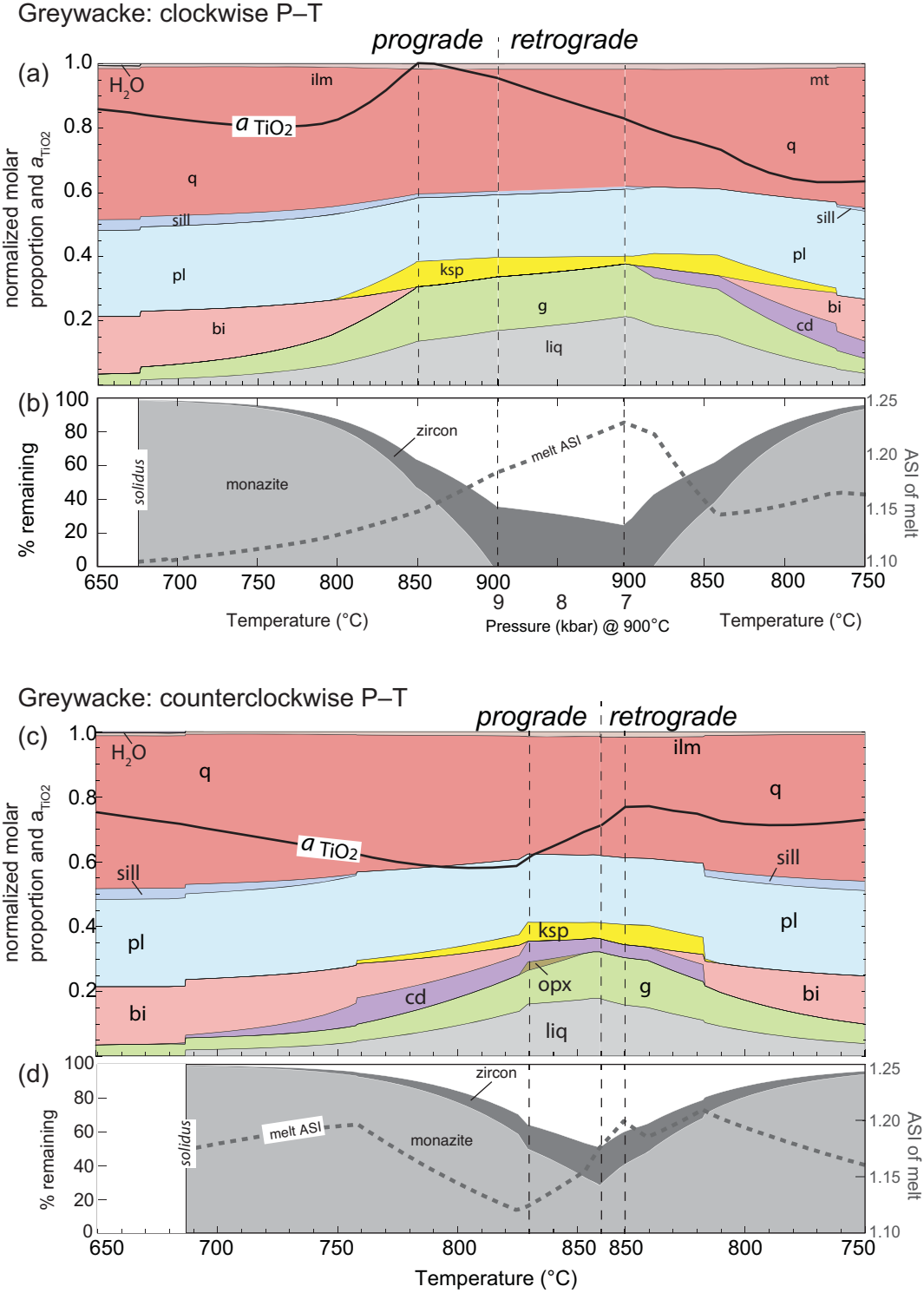
Greywacke: clockwise P–T
prograde
retrograde
(a)
normalized molar proportion and a_{TiO2}
H_2O
ilm
mt
a TiO2
q
sill
pl
ksp
g
bi
cd
liq
(b)
% remaining
solidus
monazite
zircon
melt ASI
ASI of melt
Temperature (°C)
Pressure (kbar) @ 900°C
Greywacke: counterclockwise P–T
(c)
(d)
Temperature (°C)

Figure 10

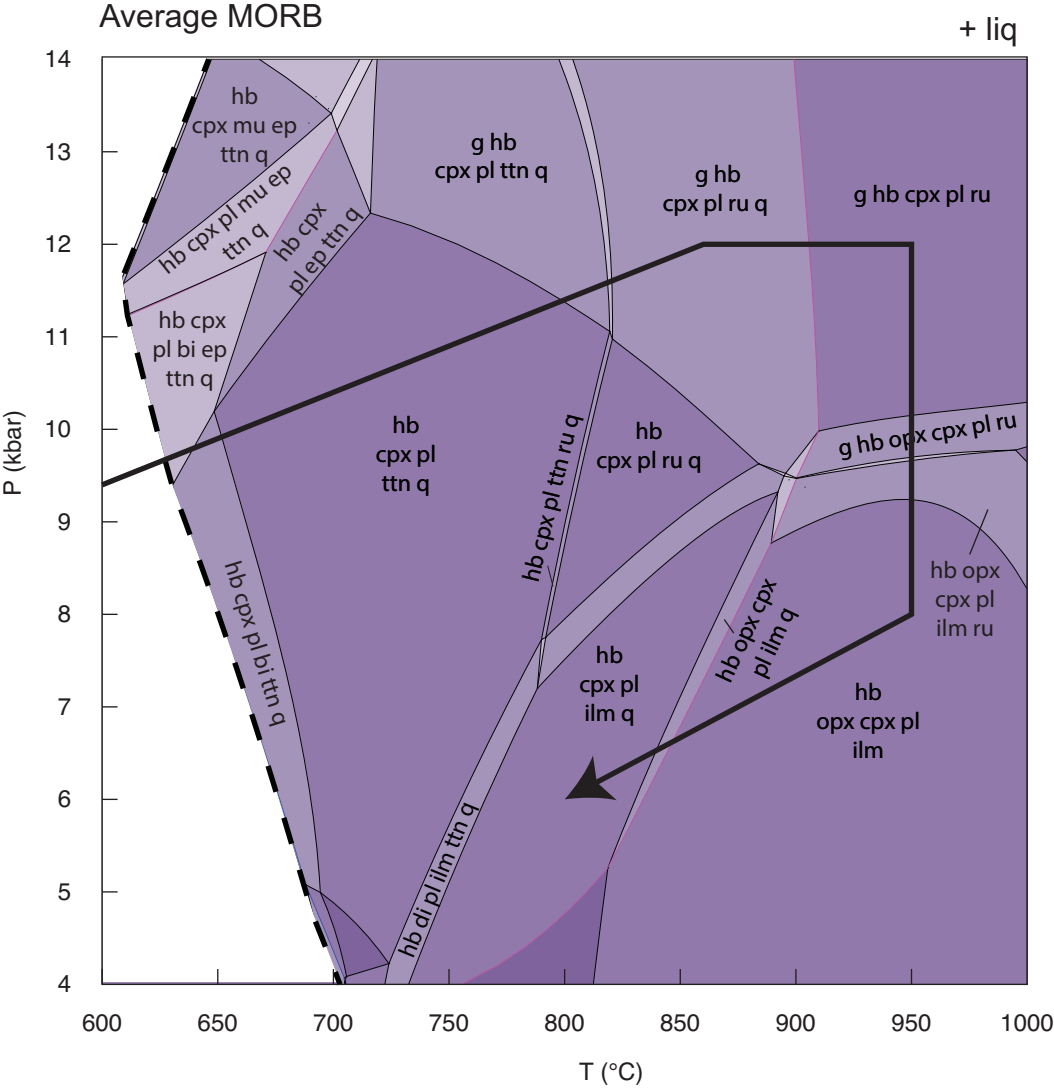
Average MORB
+ liq
hb
cpx mu ep
ttn q
hb cpx pl mu ep
ttn q
hb cpx
pl ep ttn q
g hb
cpx pl ttn q
g hb
cpx pl ru q
g hb cpx pl ru
hb cpx
pl bi ep
ttn q
hb
cpx pl
ttn q
hb cpx pl ttn ru q
hb
cpx pl ru q
g hb opx cpx pl ru
hb cpx pl bi ttn q
hb opx
cpx pl
ilm ru
hb
cpx pl
ilm q
hb opx cpx
pl ilm q
hb
opx cpx pl
ilm
hb di pl ilm ttn q
P (kbar)
T (°C)
14
13
12
11
10
9
8
7
6
5
4
600
650
700
750
800
850
900
950
1000

Figure 11

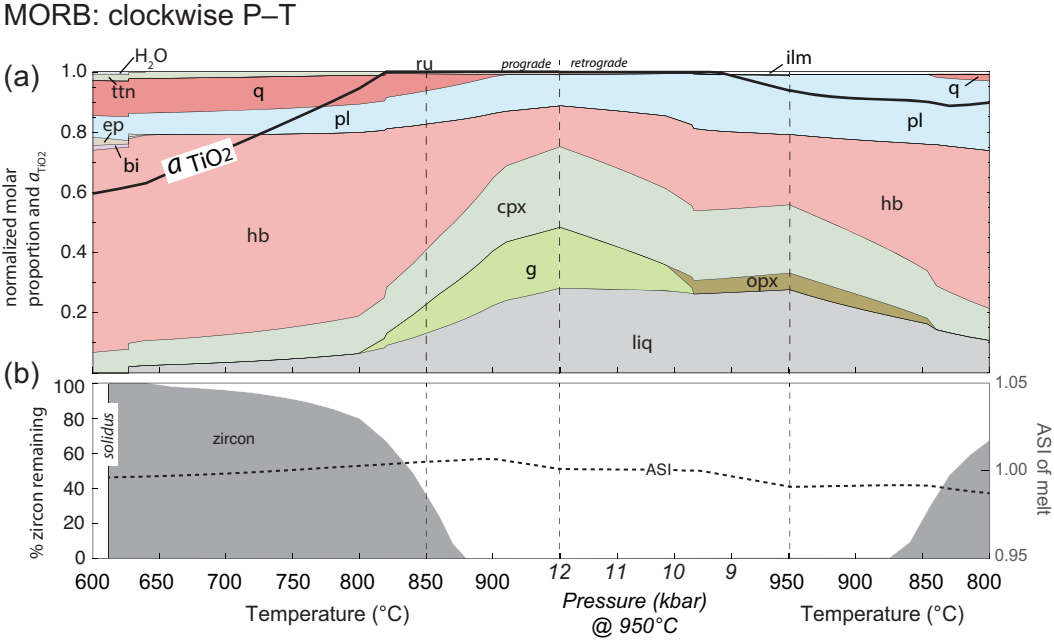
MORB: clockwise P–T
(a)
(b)
H2O
ttn
q
ru
prograde
retrograde
ilm
ep
pl
bi
a TiO2
hb
cpx
g
opx
liq
normalized molar proportion and a_{TiO2}
% zircon remaining
solidus
zircon
ASI
ASI of melt
Temperature (°C)
Pressure (kbar) @ 950°C
Temperature (°C)

Figure 12

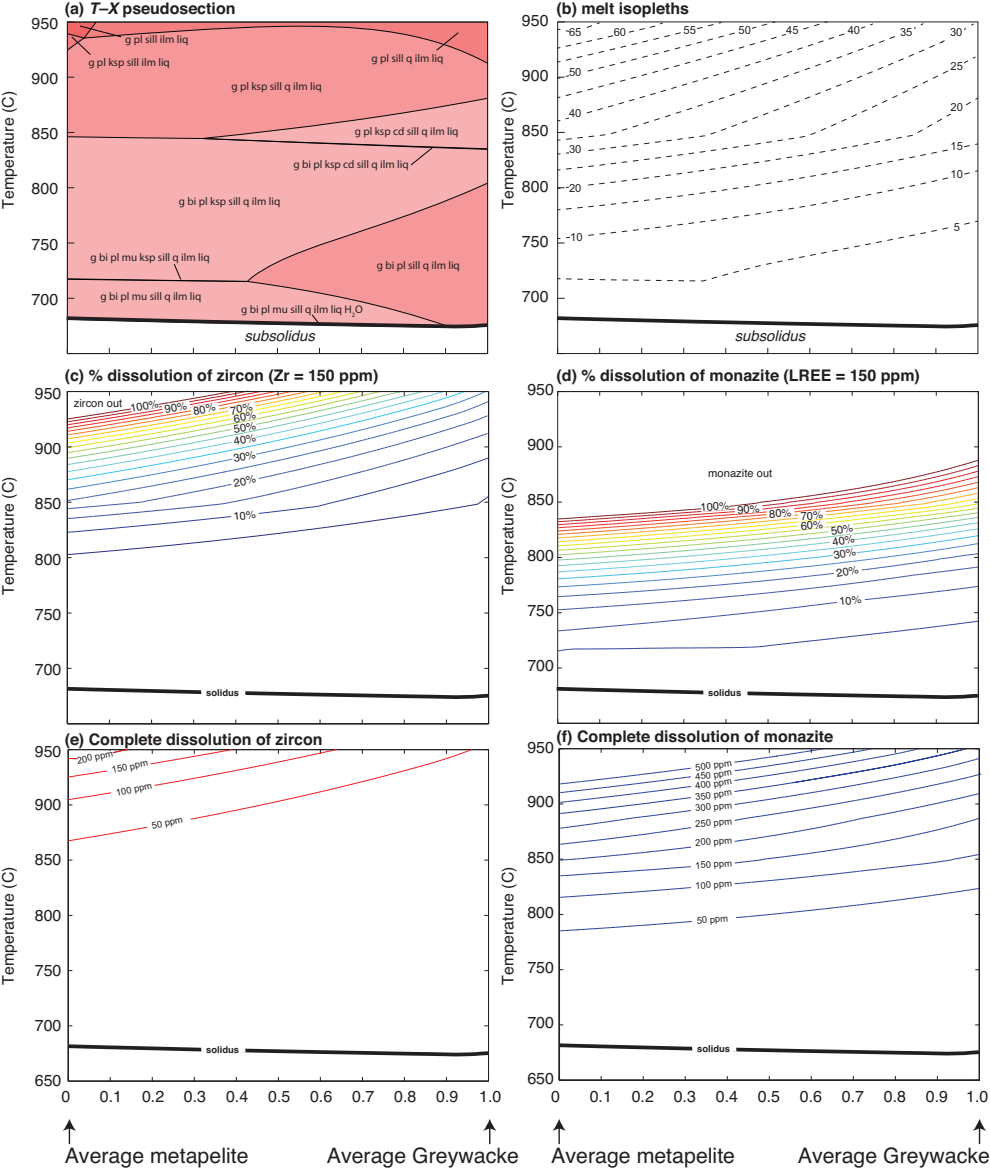
(a) T–X pseudosection
g pl sill ilm liq
g pl ksp sill ilm liq
g pl sill q ilm liq
g pl ksp sill q ilm liq
g pl ksp cd sill q ilm liq
g bi pl ksp cd sill q ilm liq
g bi pl ksp sill q ilm liq
g bi pl mu ksp sill q ilm liq
g bi pl sill q ilm liq
g bi pl mu sill q ilm liq
g bi pl mu sill q ilm liq H2O
subsolidus
(b) melt isopleths
subsolidus
(c) % dissolution of zircon (Zr = 150 ppm)
zircon out
solidus
(d) % dissolution of monazite (LREE = 150 ppm)
monazite out
solidus
(e) Complete dissolution of zircon
solidus
(f) Complete dissolution of monazite
solidus
Temperature (C)
Average metapelite
Average Greywacke
Average metapelite
Average Greywacke

Figure 13